ARMY RESEARCH LABORATORY

Computational Thermodynamics Characterization of 7075, 7039, and 7020 Aluminum Alloys Using JMatPro

by John F. Chinella and Zhanli Guo

ARL-TR-5660 **September 2011**

NOTICES

Disclaimers

The findings in this report are not to be construed as an official Department of the Army position unless so designated by other authorized documents.

Citation of manufacturer's or trade names does not constitute an official endorsement or approval of the use thereof.

Destroy this report when it is no longer needed. Do not return it to the originator.

Army Research Laboratory
Aberdeen Proving Ground, MD 21005-5069

ARL-TR-5660 **September 2011**

Computational Thermodynamics Characterization of 7075, 7039, and 7020 Aluminum Alloys Using JMatPro

John F. Chinella
Weapons and Materials Research Directorate, ARL

Zhanli Guo
Sente Software Ltd.

REPORT DOCUMENTATION PAGE	Form Approved OMB No. 0704-0188

1. REPORT DATE *(DD-MM-YYYY)*	2. REPORT TYPE	3. DATES COVERED (From - To)
September 2011	Final	1 October 2010–30 September 2011

4. TITLE AND SUBTITLE
Computational Thermodynamics Characterization of 7075, 7039, and 7020 Aluminum Alloys Using JMatPro

5a. CONTRACT NUMBER

5b. GRANT NUMBER

5c. PROGRAM ELEMENT NUMBER

6. AUTHOR(S)
John F. Chinella and Zhanli Guo*

5d. PROJECT NUMBER
1L162618AH84

5e. TASK NUMBER

5f. WORK UNIT NUMBER

7. PERFORMING ORGANIZATION NAME(S) AND ADDRESS(ES)
U.S. Army Research Laboratory
ATTN: RDRL-WMM-F
Aberdeen Proving Ground, MD 21005-5069

8. PERFORMING ORGANIZATION REPORT NUMBER
ARL-TR-5660

9. SPONSORING/MONITORING AGENCY NAME(S) AND ADDRESS(ES)

10. SPONSOR/MONITOR'S ACRONYM(S)

11. SPONSOR/MONITOR'S REPORT NUMBER(S)

12. DISTRIBUTION/AVAILABILITY STATEMENT
Approved for public release; distribution is unlimited.

13. SUPPLEMENTARY NOTES
* Sente Software Ltd., Surrey Technology Centre, 40 Occam Rd., Guildford GU2 7YG, UK

14. ABSTRACT
Thermodynamics-dependent microstructure, phase, and physical model predictions of material characteristics are demonstrated for aluminum alloys 7020 (Al-4.5Zn-1.2Mg), 7039 (Al-4.0Zn-2.8Mg), and 7075 (Al-5.6Zn-2.5Mg-1.6Cu) by direct application of Sente Software Ltd.'s Java Materials Program (JMatPro) mesoscale computation materials engineering software. JMatPro reveals phase constitutions as a function of input composition, temperature, and time; with the use of material property databases and physical models, it calculates temperature-dependent physical and mechanical properties. The JMatPro material property software provides better and more rapid understanding of materials during research, processing, product manufacture, and service. In this report, JMatPro reveals how structural and protection materials may meet design requirements for low cost, fabricability, and durability. With secondary application, the elastic bulk moduli for intermetallic phase inclusions derived from Gibbs energy by JMatPro are used to predict the maximum levels of microscale shear stresses under hydrostatic pressure. With comparison to conditions known to cause incipient spall in 7020 alloy, the levels of microscale shear stress around intermetallic inclusions are shown to equal or exceed the level of Von Mises calculated shear yield strength of 7020 alloy, revealing that deformation may occur during high load spall events, even at the initial stages of compression.

15. SUBJECT TERMS
aluminum, 7020, 7039, 7075, computational thermodynamics, JMatPro, modeling, spall

16. SECURITY CLASSIFICATION OF:			17. LIMITATION OF ABSTRACT	18. NUMBER OF PAGES	19a. NAME OF RESPONSIBLE PERSON
a. REPORT	b. ABSTRACT	c. THIS PAGE			John F. Chinella
Unclassified	Unclassified	Unclassified	UU	78	19b. TELEPHONE NUMBER (*Include area code*) 410-306-0866

Standard Form 298 (Rev. 8/98)
Prescribed by ANSI Std. Z39.18

Contents

List of Figures

List of Tables

Acknowledgments

The author would like to acknowledge the individuals of Sente Software Ltd., Dr. Zhanli Guo for JMatPro calculations, and the support of Linda Doleno and Dr. Jean-Philippe Schillé.

1. Introduction

The knowledge of phase transformations and equilibria is fundamental to material science and engineering objectives of materials development and obtaining required properties and performance. The development of new metallic alloy materials and products or alloy substitutions has provided to society and industry benefits in quality of life and improved productivity and has met increased demands in product performance, economy, durability, safety, and protection. Significant expense in personnel education and experience, as well as great experimental test effort, time, and cost are required to surmount technical barriers and concerns in the development of new materials. Further benefits and future needs of society will require even greater capabilities for accelerated development and production of improved materials and products at low cost. To meet these needs, the combination of computational thermodynamics, material models with physical and microstructural parameters, and the development of materials databases has enabled materials modeling capabilities that enhance the design, development, and application of materials (*1*). The 7XXX alloys, in part described or closely similar to the alloys of this report, are of special interest since in addition to meeting the needs of aerospace, industry, and transportation, they are extensively used or are being considered as protection materials for both welded structural and appliqué armor.

This report demonstrates application of the integrated materials modeling program, Sente Software's JMatPro (*2–5*) (see appendix), a mesoscale (*1*) program that uses computational thermodynamics and physical and microstructural models that may predict both microstructural and macroscopic characteristics of metallic materials. Traditional computational thermodynamics may predict changes in phase constitution as a function of composition and temperature, but there exists a separation of thermodynamic properties and the material properties that need be understood and accepted for use by design engineers. The theoretical models and Thermotech (*6*) materials databases in JMatPro enhance the thermodynamic calculations to make quantitative calculations possible with physical and microstructural parameters and the material properties of final interest. In this manner, JMatPro demonstrates important capabilities for accelerated materials design and development to predict both microscopic and macroscopic properties of alloys.

2. Experimental Methods and Materials

2.1 Thermodynamics, the CALPHAD Method, and JMatPro

Thermodynamics (*7–9*) involves the transfer of energy from one phase to another, with the same or different composition. It does not by itself determine absolute values of energy, structural

crystallographic features, subdivision of a second phase, or the rate of energy transfer. However, *thermodynamic modeling* is an application of statistical thermodynamics for which crystal structure must be considered (*8*) along with specific models for physical or constituent phenomena.

The CALculation of PHAse Diagrams (*CALPHAD method*) approach used in thermodynamic modeling software, including Thermo-Calc and JMatPro, may use all available experimental and theoretical data to assess the parameters of the energy models selected for each phase, and these models contain adjustable parameters that may be optimized (*8*). The CALPHAD method is based on predicting thermodynamic properties of higher order systems from those of lower component binary and ternary systems. The models that describe thermodynamic properties of phases require input of coefficients, held in databases. The Al, Ti, TiAl, Mg, and Zr alloy system thermodynamic databases of Thermotech used by JMatPro are also used in the Thermo-Calc (*10*) computational thermodynamic phase and property diagram software.

2.2 Thermodynamic Concepts

2.2.1 Gibbs Energy for Systems of Fixed Mass and Composition

The energy of most concern for reactions in metallurgy on systems that occur at constant temperature, *T*, and pressure, *P*, is the *Gibbs free energy* (G), often called the Gibbs energy, comprised of the enthalpy (H) and the entropy (S) as follows:

$$G = H - TS. \tag{1}$$

For a system to undergo a spontaneous process at constant T and P, the change in Gibbs free energy, ΔG, must be negative, and for equilibrium, ΔG must be either zero or a minimum, as follows:

$$\Delta G = \Delta H - T\Delta S. \tag{2}$$

The enthalpy represents the heat energy evolved or absorbed during the reaction, with negative indicating an *exothermic* reaction. It is determined by changes in bond energies or lattice (volume) strain because of atomic size difference as follows:

$$H = U + PV, \tag{3}$$

where U is the internal energy of the system and V is the volume. For constant temperature and pressure, the change in enthalpy equals the change of internal energy or heat of a system as follows:

$$\Delta H = \Delta U. \tag{4}$$

In practice, when dealing with solids and liquids, $H \approx U$.

Specific heat (C_p) of materials is readily available and measured and is useful for measurement of ΔH. At constant pressure, it is the quantity of heat in Joules (J) that is required to raise the temperature of a substance by 1 K, C_p, as follows:

$$C_p = \left(\frac{\partial H}{\delta T}\right)_p . \quad (5)$$

The enthalpy, or rather ΔH, can then be obtained by integration as follows:

$$H = \int_{298}^{T} C_p dT. \quad (6)$$

The entropy change ΔS, the energy not available for work or reactions of a system, is a measure of the randomness or disorder of a system and is determined primarily by changes in vibrational frequency. From a reversible process passing through equilibrium conditions at constant pressure, an increment of entropy change is defined as follows:

$$dS = \left(\frac{dH}{T}\right)_P = C_p \frac{dT}{T}; \quad (7)$$

thus,

$$\Delta S = \int_{t_1}^{t_2} C_p \frac{dT}{T} = \int_{t_1}^{t_2} C_p \, dln\, T. \quad (8)$$

S is a thermal quantity with a role similar to mass, as it can produce heat and thus work when moved from T_{high} to T_{low}. For a process to be spontaneous, $\Delta S > 0$, and for equilibrium, $\Delta S \leq 0$.

For an incremental change of state of a system of fixed mass, where work due to only a change in volume and entropy are allowed, the combination of first and second laws of classical thermodynamics gives the change of internal energy (*9*) as follows:

$$dU = TdS - PdV. \quad (9)$$

For a system of fixed mass and composition, the differentiation of equation 3 with a combination of equation 9 gives changes in H as follows:

$$H = U + PV; \text{ thus, } dH = TdS + VdP. \quad (10)$$

Again, for a system of fixed mass and composition, when temperature and pressure vary and with use of equation 10, the change in G is as follows:

$$G = H - TS; \text{ thus, } dG = -SdT + VdP. \quad (11)$$

The latter relation, with variables of T and P, is often more convenient than equation 9 or 10.

2.2.2 Gibbs Energy With Variation of T, P, Component Size, and Composition

When variation of the composition and size of the system may occur, G is a function of T, P, and the number of moles of all component species present in the system are as follows:

$$G = G(T, P, n_i, n_j, n_k, \ldots), \quad (12)$$

where n_i, n_j, n_k,… are the numbers of moles of the components i, j, k,… present in the system, and the state of the system is fixed only when all these independent variables are fixed. Partial differentiation of the G, equation 12, is as follows:

$$dG = \left(\frac{\delta G}{\delta T}\right)_{P, n_i, n_j, \ldots} dT + \left(\frac{\delta G}{\delta P}\right)_{T, n_i, n_j, \ldots} dP + \left(\frac{\delta G}{\delta n_i}\right)_{T,P,n_j, n_k, \ldots} dni + \left(\frac{\delta G}{\delta n_j}\right)_{T,P,n_i, n_k, \ldots} dnj + \text{etc.} \quad (13)$$

If the mole numbers of the components remain constant during the process, then equation 13 simplifies to equation 11, dG = –SdT + VdP, from which

$$\left(\frac{\delta G}{\delta T}\right)_{P, n_i, n_j, \ldots} = -S \quad (14)$$

and

$$\left(\frac{\delta G}{\delta P}\right)_{T, n_i, n_j, \ldots} = V. \quad (15)$$

Substitution in equation 13 is as follows:

$$dG = -SdT + VdP + \sum_{i=1}^{i=k} \left(\frac{\delta G}{\delta n_i}\right)_{T,P,n_{j,\ldots}} dn_i, \quad (16)$$

where $\sum_{i=1}^{i=k} \left(\frac{\delta G}{\delta n_i}\right)_{T,P,n_{j,\ldots}} dn_i$ is the sum of k terms, each of which is obtained by differentiating G with respect to the number of moles of the ith component at constant T, P, and n_j, where n_j represents the number of moles of every component other than the ith component.

2.2.3 Gibbs Partial Free Energy and Chemical Potential

The term $\left(\frac{\delta G}{\delta n_i}\right)_{T,P,n_j,\ldots}$ of equations 13 and 16 is the chemical potential of the component i and is designated as μ_i, as follows:

$$\mu_i = \left(\frac{\delta G}{\delta n_i}\right)_{T,P,n_j}. \quad (17)$$

The chemical potential of equation 17 is alternatively called the partial molar Gibbs free energy $\bar{G}$. It is defined as the increase in the Gibbs free energy of the system for a small addition of the component i per mole of i added, with addition being made at constant T and P and numbers of all other components present. Equation 13 can thus be written as follows:

$$dG = -SdT + VdP + \sum_1^k u_i dn_i, \quad (18)$$

or more simply as

$$dG = -SdT + VdP + \sum \mu_i dn_i. \quad (19)$$

In equation 19, G is a function of the independent, intensive variables T, P, and composition. These intensive properties are measures of the following potentials: temperature for heat intensity, pressure for massive movement, and chemical for tendency for component i to leave the phase. Existence of a chemical-potential gradient is the driving force for chemical diffusion, and equilibrium occurs when the components are distributed throughout the phases such that a components chemical potential is the same in all phases.

2.2.4 Activity

The chemical potential for *any solution* may be described for convenience by defining the *activity* of a component, a_i, a parameter that describes the availability, or tendency of an atom to leave a solution, such that the chemical potential of a component may be described as follows:

$$\mu = G + RT \ln a_i. \tag{20}$$

In the simple case of ideal solutions for which bond energies of all atoms are identical on mixing, the $\Delta H_{mix} = 0$, and the free energy change on mixing is due solely to the change in S as follows:

$$\Delta G_{mix} = -T\Delta S_{mix}. \tag{21}$$

It follows from statistical thermodynamics and configuration states that the mole fractions, $X_i = X_A, X_B$, of components for a binary ideal solution and the chemical potentials are as follows:

$$\mu_A = G_A + RT \ln X_A, \tag{22}$$

and

$$\mu_B = G_B + RT \ln X_B, \tag{23}$$

where G_A and G_B are G values of pure components and R is the universal gas constant. Therefore, the activity, a_i, of a component in any ideal solution is equal to its mole fraction, X_i, as follows:

$$a_i = X_i. \tag{24}$$

In addition to describing the free energy curve, equations 19–24 describe the relationship of the chemical potentials and activities to mole fractions of constituents for an ideal solution.

In any non-ideal solution, the activities of the components are not equal to their mole fractions, and it is convenient to define a thermodynamic function called the *activity coefficient*, the ratio of the activity of the component to its mole fraction, as follows:

$$\gamma_i = \frac{a_i}{X_i} \tag{25}$$

for ideal reactions to solution $\gamma_i \cong 1$. For $\Delta H_{mix} < 0$, heat is evolved into the solution, the reaction is exothermic, the activity is <1, and $\gamma_i < 1$. For $\Delta H_{mix} > 0$, the reaction occurs with heat absorption from the solution, the process is called *endothermic*, the activity is >1, and $\gamma_i > 1$. The

activity and activity coefficient are important thermodynamic parameters required for determination of equilibrium states of components in solution.

2.3 JMatPro Temperature Step Calculations

JMatPro standard program temperature step (TS) calculations of thermodynamic equilibrium properties include the following: (1) percent phases, (2) percent elements in specific phases, (3) element distribution in phases, (4) weight-percent phases at temperature, (5) partial Gibbs energy, (6) activity α_i, (7) heat capacity or specific heat, Cp, and (8) total or phase details of H, G, and S. Calculation types 1–3 include numerical start and finish values of temperature stability of equilibrium phases and the relative percents of phases or elements for each TS or transformation temperature.

Beyond predicting phase diagrams for which CALPHAD is known, JMatPro (*2–5*) computationally links CALPHAD (*11*) phase diagrams and thermochemical Gibbs phase energy minimization routines for multicomponent alloys used in industrial practice to calculate the phase transformations, microstructures, and properties that may be obtained during conditions of processing or service that are of interest to engineers and scientists. It includes subroutines for automatic start points and algorithms to ensure reliable results for multicomponent multiphase equilibria and for checking stability of phases that may have miscibility gaps or potential for ordering. It can derive thermophysical properties from Gibbs energy and perform calculations for phases and properties under non-equilibrium conditions of solidification during continuous cooling by use of the Scheil-Gulliver (*2–5*, *7*) model.

JMatPro has reliable routines for finding phase boundaries and for TS map plots of properties, stable or metastable phases, or elemental composition vs. temperature. Mechanical properties of hardness, flow stress, and strain may be calculated. The maximum solubility of elements may be clearly observed, along with solubility curves and phase relationships for each element or phase as a function of temperature so that alloy selection or process techniques may then be applied to optimize phase contents and the alloy properties and performance.

2.4 JMatPro Calculations of Thermophysical and Mechanical Properties

CALPHAD information with JMatPro may be used to calculate thermophysical (*7–9*) properties, including Young's (E), shear (G_m), and bulk (K) moduli, Poisson's ratio, thermal conductivity, thermal expansion coefficient, density, molar volume, and electrical conductivity (see appendix, formulas A1–A9). Comparisons of computational and experimental results have revealed excellent agreement for elastic moduli and thermal conductivity, including temperature dependence and effect of microstructure (*2–5*). Volume fractions and compositions are predicted and may be combined with properties of each phase drawn from a separate materials database, and there is a choice of materials models that take into account microstructural parameters such as grain or particle size. The process parameters of temperature and time may be selected to simulate effects on microstructure during annealing, solution treating, quenching, and tempering.

2.5 JMatPro Calculations of Phase Transformations and Metastable Phase Equilibria

Although equilibrium calculations provide valuable information for processing through liquidus and solidus temperatures and phase solubility curves, in practice, the conditions for equilibrium (*12*),

$$L^2 << D_s t, \tag{26}$$

where L is the length solidified, D_s is the diffusion coefficient of solute in the solid, and t is time, may not be achieved. Furthermore, many Al alloys are hardened by metastable phases, so it is important that thermodynamic calculations be able to include metastable phases for understanding and predicting equilibria and hardening and as input into kinetic equations to calculate time and temperature conditions for phase formations. JMatPro calculations have been successful in the area of phase transformations, and in time temperature transformation (TTT) and continuous cooling transformation (CCT) diagrams. The main approach utilizes the well-known Johnson-Mehl-Avrami (*2*, *7*) equation as follows:

$$V_{tr}/V_{max} = 1 - exp\left(-\frac{\pi}{3} N_r G_r^3 t^n\right), \tag{27}$$

where V_{tr} is the volume fraction transformed, V_{max} is the equilibrium volume fraction of that phase, N_r is the rate of nucleation per unit volume, G_r is the growth rate, t is the transformation time, and n depends on growth morphology that includes shape and growth rate. For spherical particles, n = 1. Heterogeneous nucleation may be taken into account by use of a wetting angle function. Activation energy may be taken into account for rapidly quenched alloys.

The general form of the equation often used in practice is

$$x = 1 - \exp(-kt^n), \tag{28}$$

where k is a constant empirically evaluated at each temperature, and n is the Avrami exponent evaluated empirically, generally between 1 and 4. This thermodynamic model includes a premise that GP zones are formed due to a miscibility gap in the Al-rich phase. A correction factor is necessary to lower GP solvus temperatures from the effect of interface elastic strain energy of coherent Al-Cu that is proportional to the Cu concentration.

2.6 Applications of JMatPro

Important material properties are connected to the stable forms of precipitates that result from solutionizing, annealing or intermediate heat treatment, and phase formation during nonequilibrium solidification processing. With aluminum and (specifically) 7XXX alloys, CALPHAD and JMatPro have the capability to reveal important information on stable and metastable forms of precipitation, the role of constituent elements, and the role of minor elements often considered as insoluble compounds.

Solidification of the commercial foundry and wrought ingot Aluminum Association (AA) Cu 2XXX, Mn 3XXX, Si 4XXX, Mg 5XXX, Mg-Si 6XXX, and Zn-Mg-(Cu) 7XXX alloys largely occurs with a eutectic and dendritic nature (*7*) so that even small amounts of impurities or minor elements may give rise to unwanted intermetallic phases. The complex solidification paths and transitions between intermetallics have been shown to be predicted with a high degree of accuracy in Al alloys using the Scheil-Gulliver model of JMatPro (*3*–*5*) that uses an assumption that no back diffusion to the liquid occurs in the primary or secondary phases formed during the solidification process. For eutectic systems, this solidification process occurs such that the solid phase in the center of dendrites is lean in solute, with the liquid becoming more enriched in solute as solidification occurs. The L + $\propto$ or L + β composition of the liquid eventually reaches that of the eutectic and final solidification occurs by a eutectic reaction as follows:

$$L \rightarrow \alpha + \beta. \tag{29}$$

Comparisons of experimental data and the Scheil-Gulliver model-predicted fraction solid vs. temperature plots for Al alloys have shown excellent agreement. A significant advantage of using a thermodynamic approach to solidification is obtaining the heat evolution and the values of C_p during solidification, and it has been shown that comparison of the experimental latent heat and calculated Cp values are in agreement such that calculated values may be reliably used (*4*).

One of the largest applications of aluminum is can body stock, made of 3000 series alloys. During solidification of 3004 (Al-1.2Mn-1.0Mg) and 3104 (Al-1.1Mn-1.0Mg) alloys, the predominant phase formed during solidification is Al_6Mn (*3*, *4*). An important objective of processing 3000 alloys is solution treatment and breakdown, or partial breakdown of $Al_6(FeMn)$ or Al_6Mn intermetallic phase, to alpha (α) AlFeMnSi. The surface finish of 3104HXX tempered alloy is much improved if α particles rather than Al_6Mn predominate, so it is important to optimize processing to obtain the α. There is competition between α and Mg_2Si as the temperature is lowered and Mg_2Si is formed over preference to α, lowering the amount α (see figure 1). During heating of equilibrium microstructures from ambient conditions for high temperature solution treatment, microconstituent Mg_2Si in the 3104 alloy may act as nucleation sites for α AlFeMnSi that grow by the release of Si from dissolving Mg_2Si. Experimental results and CALPHAD temperature vs. percent phase plots show good agreements of experimentally observed and JMatPro predictions of Mg_2Si, Al_6Mn, and α phase for AA3104 (*4*).

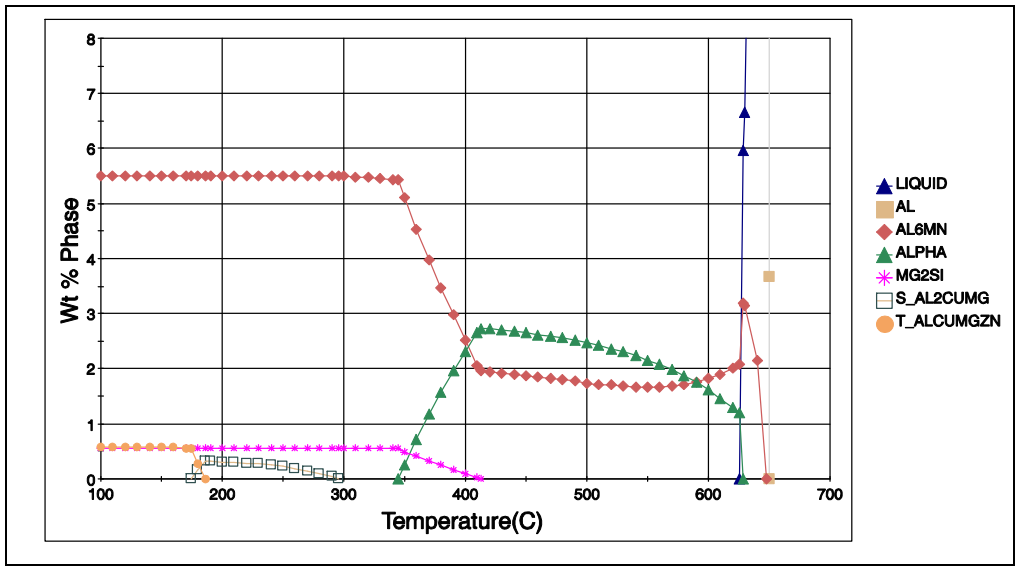

Figure 1. JMatPro TS equilibrium phase calculations for Al 3104.

2.7 Hardening Precipitates in Al-Zn-Mg-(Cu) 7XXX Alloys and the Effect of Zn/Mg Ratio

The highly soluble alloy elements in the quaternary Al-Zn-Mg-Cu 7XXX system allow high levels of solute to be taken into solution and for age hardening treatments to produce reactions for high hardness and flow strength. These alloys have remained in use and have been the subject of research for many years and have complex Al-Zn-Mg-(Cu) metallurgical behaviors that enable a wide range microstructures and material properties by design (*4, 12, 13*).

In practice, 7XXX alloys achieve maximum hardness due to precipitation of the metastable phases related to stable counterparts of η, T, and S. The stable phase compositions are (1) η, based on the binary $MgZn_2$ Laves compound but also of $Mg(AlCu)_2$; (2) T, AlCuMgZn that exists in Al-Zn-Mg and Al-Zn-Mg-Cu systems; and (3) S, Al_2CuMg present in Al-Zn-Mg-Cu and Al-Cu-Mg systems, as with alloy 2024. For η phase equilibrium alloys, the actual nucleation modes (*13–19*) and precipitation mechanisms of the Al-Zn-Mg alloys are determined by the process and quench conditions and any heterogeneities of constituent phases, dispersoids, and grain or subgrain boundaries that may be present. With dependence on quench conditions from supersaturated solid solution, there appear to be the following three possible precipitation reactions (*14*): (1) solid solution → η, (2) solid solution → GP, and (3) solid solution → ή → η. The ή is believed to be formed by two mechanisms, either starting from vacancy rich clusters (VCRs) and then to intermediate GP(II) zones to ή or from solute rich cluster GP(I) zones that either undergo dissolution or reach a critical size before transforming to ή. The sequence of reactions, called duplex aging, which is used in industrial practice and for which optimum properties may be obtained, is solid solution → GP → ή (*19*). The GP zones contribute hardness. The incoherent lattice-precipitate stable η phase does not contribute age hardening.

Since alloy 7075 is known to be processed with high quench rates and the 7020 is known to be processed with slow quench rates, there may be likely differences in nucleation mechanisms that are dependent on either vacancies or solute clusters.

In 7XXX alloys, the Zn/Mg ratio is considered most critical to deciding the type of precipitation reaction and phase that takes place, and a Zn/Mg ratio of 2.0 is considered the critical value below which T is favored over η (*4*, *19*). In addition to levels of Mg and combined levels of Zn + Mg, the Zn/Mg ratio has also been proposed to determine the material properties and microstructures that affect resistance to stress corrosion cracking (SCC) of these alloys (*19*, *20*). When significant levels of Cu are added to 7XXX alloys, the phase stability and the hardening effect beyond the solution effect of the η phase may be enhanced, and when the precipitate structure is overaged, improved resistance to SCC may be achieved (*21*).

CALPHAD calculated temperature plots vs. phase contents of η, T, and S, as well as ε AlCrMnMg and Mg_2Si, have been demonstrated (*4*, *19*) for a series of high-strength 7XXX alloys 7049, 7050, 7075, and 7079 (*22*) (see table 1). The 7049 alloy represents the highest Zn/Mg ratio at 3.14, and the equilibrium phase is almost completely η. The 7050 Zn/Mg ratio is at 2.76, and the equilibrium phase remains substantially all η, but there is also significant S phase present due to the high copper content. The 7075 alloy has a lower Zn/Mg ratio of 2.3 and predominately contains η along with S Al_2CuMg. The effect of low Cu in 7075 is shown to allow some T phase below 200 °C, along with a low level of S phase. Al 7079 has the lowest Zn/Mg ratio at 1.30, and the precipitation is largely T, along with small amounts of η and Mg_2Si. Effectively, the Zn/Mg ratio is also dependent on the level of free Mg available among potential η, S, and Mg_2Si phase reactions.

Table 1. Aluminum association registration, alloy chemistry, and Zn/Mg ratio.

Alloy	Year/By	Zn/Mg	Si	Fe	Cu	Mn	Mg	Cr	Zn	Ti	Zr	Ti + Zr
7049	1968 U.S.	3.14	0.25	0.35	1.2 1.9	0.20	2.0 2.9	0.10 0.22	7.2 8.2	0.10	—	—
7050	1971 U.S.	2.76	0.12	0.15	2.0 2.6	0.10	1.9 2.6	0.04	5.7 6.7	0.06	0.08 0.15	—
7075	1954 U.S.	2.24	0.40	0.50	1.2 2.0	0.30	2.1 2.9	0.18 0.28	5.1 6.1	0.20	—	—
7079	Reclass.	1.30	0.30	0.40	0.40 0.80	0.10 0.30	2.9 3.7	0.10 0.25	3.8 4.8	0.10	—	—

New generations of advanced, high-performance aircraft include forgeable aluminum alloys of the ή-strengthened, high-strength Al-Zn-Mg-Cu alloys 7085 and 7037 (*22*) (see table 2). The ή-strengthened, Al-Zn-Mg medium-strength alloys are also used for advantage in vehicular and structural applications (see table 3).

Table 2. New advanced, high-performance/durability Al-Zn-Mg-Cu alloys, ή strengthened.

Alloy	Year/By	Zn/Mg	Si	Fe	Cu	Mn	Mg	Cr	Zn	Ti	Zr	Ti + Zr
7085	2002 U.S.	5.00	0.06	0.08	1.3 2.0	0.04	1.2 1.8	0.04	7.0 8.0	0.06	0.08 0.15	—
7037	2006 Ger.	4.94	0.10	0.10	0.60 1.10	0.50	1.3 2.1	0.04	7.8 9.0	0.10	0.06 0.25	—

Table 3. Al-Zn-Mg ή alloy examples presently used for industrial and vehicular applications.

Alloy	Year/By	Zn/Mg	Si	Fe	Cu	Mn	Mg	Cr	Zn	Ti	Zr	V
7204	2005 Japan	3.00	0.10	0.10	0.20	0.20 0.70	1.0 2.0	0.30	4.0 5.0	0.20	0.25	0.10
7003	1975 Japan	7.67	0.30	0.35	0.20	0.30	0.50 1.0	0.20	5.0 6.5	0.20	0.05 0.25	—
7108	1983 U.S.	4.76	0.10	0.10	0.05	0.05	0.70 1.40	—	4.5 5.5	0.05	0.12 0.25	—

2.8 Aluminum Alloy Materials 7020, 7039, and 7075 and JMatPro Calculations

Materials examined through this demonstration of JMatPro include the alloys/AA registration years Al-4.5Zn-1.2Mg 7020 (1972), Al-4.0Zn-2.8Mg 7039 (1962), and Al-5.6Zn-2.5Mg-1.6Cu (1954) (see table 4) (*22*). Chemical compositions of these alloys used in JMatPro calculations were either from producer certificates for ISO EN-485 7020-T651 plates (*23*), obtained from registration chemistry and literature for 7039 (*22*, *24*), or for 7075, provided by Sente Software (see table 4). Alloys 7039 and 7020 serve as structural armor (*24*, *25*). Performance measures of the structural armors include low cost and capabilities for ballistic and blast protection, weld fabricability, and durability against SCC and exfoliation corrosion (EXC). Alloy 7075 continues to serve wherever its high strength may be exploited, primarily as an aerospace material (*12*, *26*). The T7XXX overage tempers of 7075 and 7020 provide significant improved resistance to SCC over the T6XXX condition (*12*, *19*, *21*).

Table 4. Aluminum association registrations and alloy chemistries in JMatPro calculations.

Alloy	Date/By	Zn/Mg	Si	Fe	Cu	Mn	Mg	Cr	Zn	Ti	Zr	Ti + Zr
7020	1972 Eur. Al Ass.	3.75	0.35	0.40	0.20	0.05 0.50	1.0 1.4	0.10 0.35	4.0 5.0	—	0.08 0.20	0.08 0.25
7039	1962 U.S.	1.43	0.30	0.40	0.10	0.10 0.40	2.3 3.3	0.15 0.25	3.5 4.5	0.10	—	—
7075	1954 U.S.	2.24	0.40	0.50	1.2 2.0	0.30	2.1 2.9	0.18 0.28	5.1 6.1	0.20	—	—
Chemistries Used in the JMatPro Calculations												
Alloy	**Ref.**	**Zn/Mg**	**Si**	**Fe**	**Cu**	**Mn**	**Mg**	**Cr**	**Zn**	**Ti**	**Zr**	**Other**
7020	(*23*)	3.60	0.10	0.26	0.16	0.25	1.24	0.17	4.47	0.03	0.13	0.01
7039	(*24*)	1.48	0.13	0.20	0.05	0.24	2.87	0.19	4.25	0.02	0.01	0.24 Ni
7075	JMatPro	2.24	0.40	0.50	1.6	0.30	2.5	0.23	5.6	—	—	—

Results of this report include Thermo-Calc Al-Zn-Mg ternary diagrams prepared from the Thermotech TTAL6 database (see appendix) and JMatPro TTT and CCT curves and temperature step calculations. The TS standard calculations include plots of the following: (1) partial Gibbs energy ($\overline{G}$) of elements in the alloy, (2) activity, a_i, (3) weight-percent element composition of the liquid phase, (4) H, S, and G of equilibrium phases in 7020 alloy, (5) weight-percent of phases, (6) phase distribution plots at temperature, (7) weight-percent of individual Cu element in all phases, (8) weight-percent of all elements of individual constituent and hardening phases, and (9) thermophysical properties of shear and bulk moduli for 7075 alloy.

An example of an indirect application of thermophysical properties (*7–9*) is shown by use of the JMatPro calculated elastic bulk moduli for constituent particles of Al-Zn-Mg-Cu 7075 (here extrapolated to 7020), together with the models of Das and Radcliffe (*27*) and Ashby et al. (*28*) to predict the maximum level of hydrostatic pressure-induced (*29*) microscale shear stress around constituent particles. These shear stresses are compared to the Von Mises criterion (*30*) predicted levels of root-mean shear stress obtained from certificate or experimental values of yield strength in tension of 7020 and 7075 and the experimental and theoretical stress—time dependent levels of the thermodynamic controlled fracture model of Chevrier and Klepaczko (*31, 32*) that describe conditions for incipient spall of Al-Zn-Mg 7020 aluminum and aluminum and steel alloys.

3. Experimental Results and Discussion

3.1 Thermo-Calc Phase Ternary Diagram Predicted by Thermotech Al Database

A ternary Al-Zn-Mg phase diagram at 160 °C with 10-weight-percent limits for Zn and Mg (see figure 2) with Al-Zn-Mg superposed chemistries for 7020 and 7039 Al alloys reveal equilibrium phases of the alloys. The regions' crystal lattice structures are as follows: Al_3Mg_2 + FCC_A1, Al_3Mg_2 + FCC_A1 + T-AlCuMg, FCC_A1 + T-AlCuMg, FCC_A1 + $MgZn_2$ + T-AlCuMg, FCC_A1 + $MgZn_2$, and FCC_A1 + HCP_A3 +$MgZn_2$. The A1 and A3 symbol nomenclatures are the "Strukturbericht" crystal structures, respectively, for the sequentially named and classified prototypes of the *Cu* face centered cubic (FCC), and *Mg* hexagonal close packed (HCP) crystal phase structures. The Al_3Mg_2, AlCuMg, and $MgZn_2$ are molecular formulas of the other phases present. The 7020 chemical composition appears at the boundary of the Al + η $MgZn_2$ and Al + $MgZn_2$ + T AlCuMg equilibrium phase regions. The 7039 (and Al-4.6Zn-2.5Mg 7017) chemical compositions are within the Al + T equilibrium phase regions. The Al + T precipitate alloys in T6 conditions are known to have service concerns of low resistance to SCC. With select process techniques and duplex T6 or T7 hardening tempers that shift the precipitate structure more toward the equilibrium phase, significant resistance to SCC may be obtained with the Al + η 7020 and 7075 alloys.

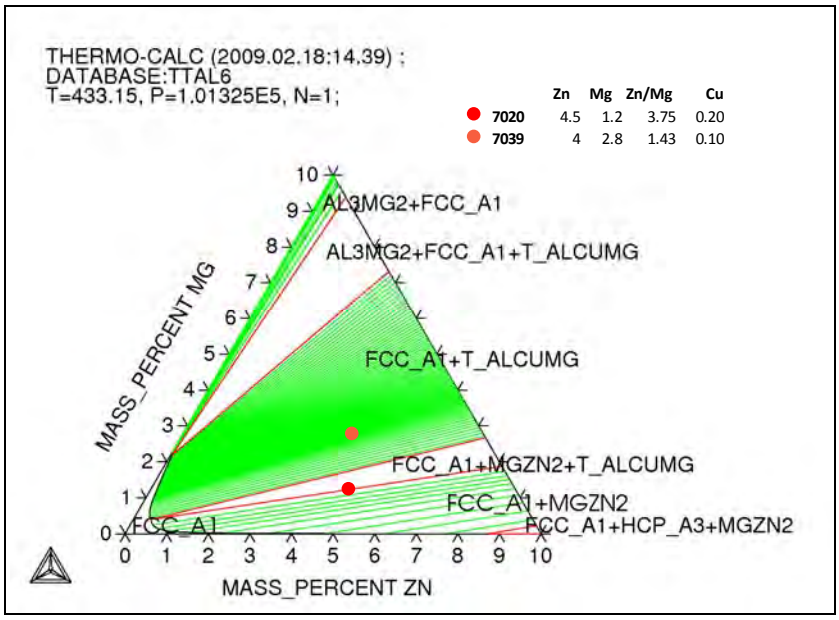

Figure 2. Thermo-Calc ternary Al-Zn-Mg phase diagram calculated at 160 °C with superposed 7020 and 7039 compositions (see text for explanation of phases and nomenclature).

A ternary Al-Zn-Mg phase diagram at 325 °C (see figure 3) reveals that 7020 Al + η phase alloy undergoes phase dissolution at lower temperatures than the Al + T alloy 7039. It also appears that the Al + $MgZn_2$ + T fields (η = $MgZn_2$) diminish, and the Al + $MgZn_2$ and Al + T + AlCuMg fields become more prominent. The phase diagram predicted behavior is consistent with weld fabrication behavior of 7020, where the η precipitates tend to dissolve rather than overage during reheat and then harden by natural aging at room temperature to achieve mechanical properties of high yield strength and strain hardening with good ductility to levels of high tensile strength (*19*). Unlike 7020, the cold-work-hardened Al-Mg alloys may typically lose 40%–50% of their yield strength following welding (*19*). As an ή-strengthened alloy, the chemistry of 7020 appears to achieve a more optimal Mg content for strengthening while maintaining low contents of Mg + Zn.

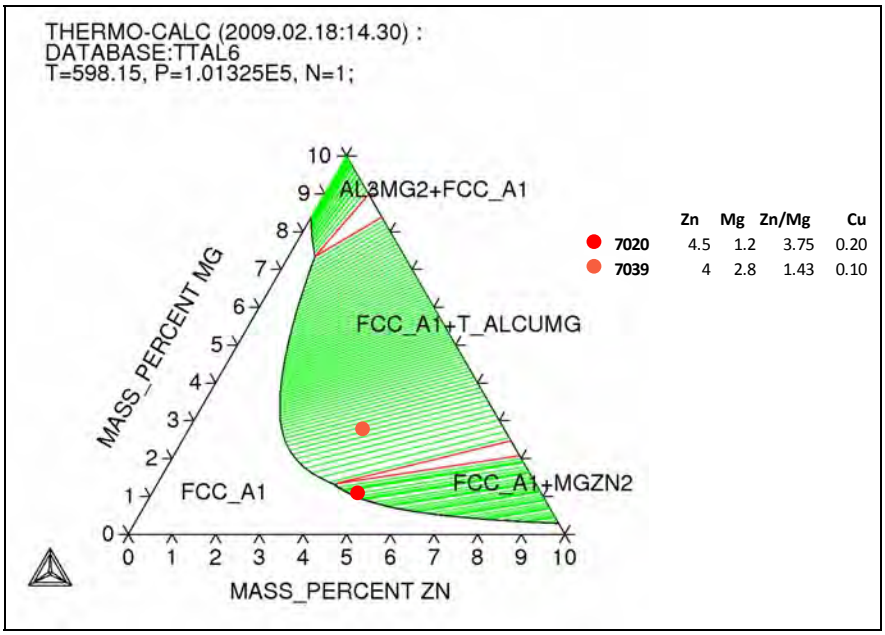

Figure 3. Thermo-Calc ternary Al-Zn-Mg phase diagram calculated at 325 °C with superposed 7020 and 7039 Zn and Mg mass (weight) percent.

3.2 JMatPro Time-Temperature-Transformation and Continuous-Cooling-Transformation Curves

TTT curves (*7*) are beneficial to predicting schedules of solution and age-hardening heat treatments. CCT (*7*) curves are of interest to determine allowable cooling rates and intervals, either to obtain desired microstructures or avoid deleterious precipitates in cooling castings or during quench processes following solution treatment of wrought alloys (*2–4*) to avoid residual stress or distortion. Table 5 reveals a summary of approximate critical times and temperatures for 0.5 weight-percent of phase precipitation in JMatPro calculated TTT and CCT curves for 7020, 7039, and 7075 (see figures 4–9). The CCT curves (with their superposed rates of cooling) clearly describe relationships of cooling and microstructure. Calculated times for start of precipitation of GP solute-rich clusters (*7, 12, 15–19*) appear to follow the concentration of Mg such that the low Mg alloy 7020 has longer periods and high Mg alloy 7039 has short periods. The temperatures of the nose of TTT C-curves and the CCT quench rates required for avoidance of initiating GP or metastable phases appear to increase with the total Zn + Mg solute content of these alloys (see table 5), and the higher Cu content of 7075 appears to provide temperature stability to the η phase of 7075. The CCT curves reveal that initiation times for all major phases for 7020 exceed those for 7039 and 7075 and low sensitivity of the 7020 phases to rates of cooling or quench processes, which is important to avoid potentially non-optimal precipitation hardening before the designed hardening process with Mg and Zn. The low sensitivity of 7020 to slow cooling rates also provides capability to avoid residual stress that may lead to both dimensional changes during fabrication and may introduce a necessary condition for SCC.

Table 5. JMatPro TTT and CCT curve critical times and temperatures of 7020, 7039, and 7075.

Alloy	Mg (Weight-Percent)	(Zn + Mg) (Weight-Percent)	TTT Nose			CCT Cool Rate Minimum (°C)/s
			Phase	Time (s)	Temp. (°C)	
7020	1.2	5.7	GP	30	108	1
			ή	200	250	—
			η	8000	275	—
7039	2.8	6.8	GP	6	125	5
			T′	130	275	—
			T	2900	315	—
7075	2.5	8.1	GP	14	140	10
			ή	40	320	—
			S’	80	320	—
			T′	230	280	—
			η	2300	350	—

Note: GP = Guinier-Preston element-rich cluster zone (*7*).

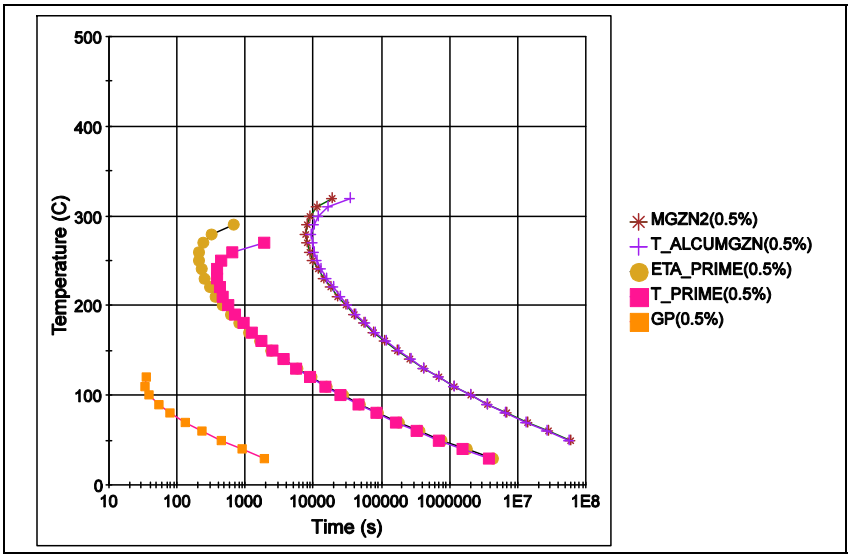

Figure 4. JMatPro calculated TTT curve for 7020 (start temperature = 500 °C).

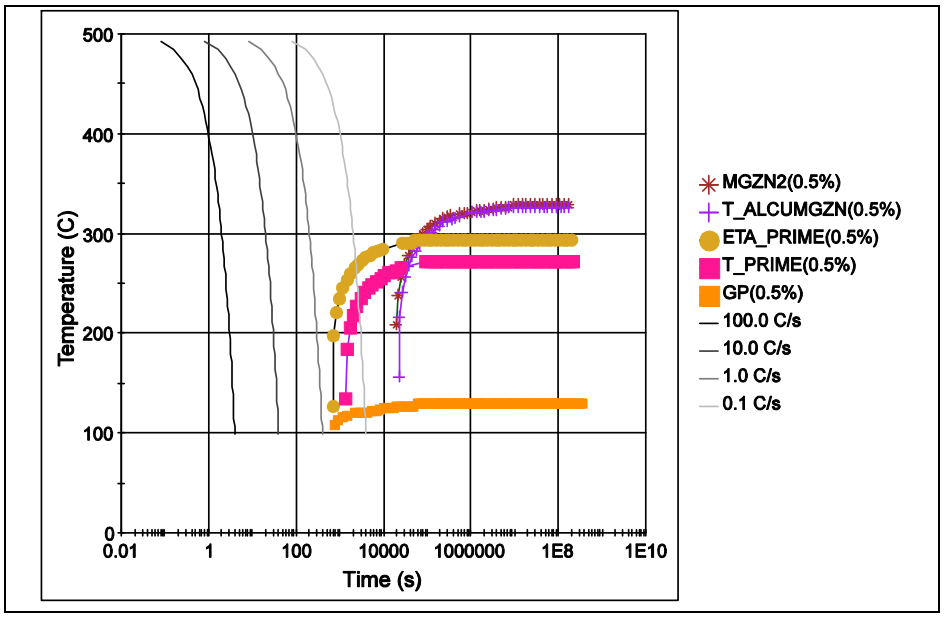

Figure 5. JMatPro calculated CCT curve for 7020 (cooling rate curves left to right are 100.0, 10.0, 1.0, and 0.10 °C/s, and start temperature = 500 °C).

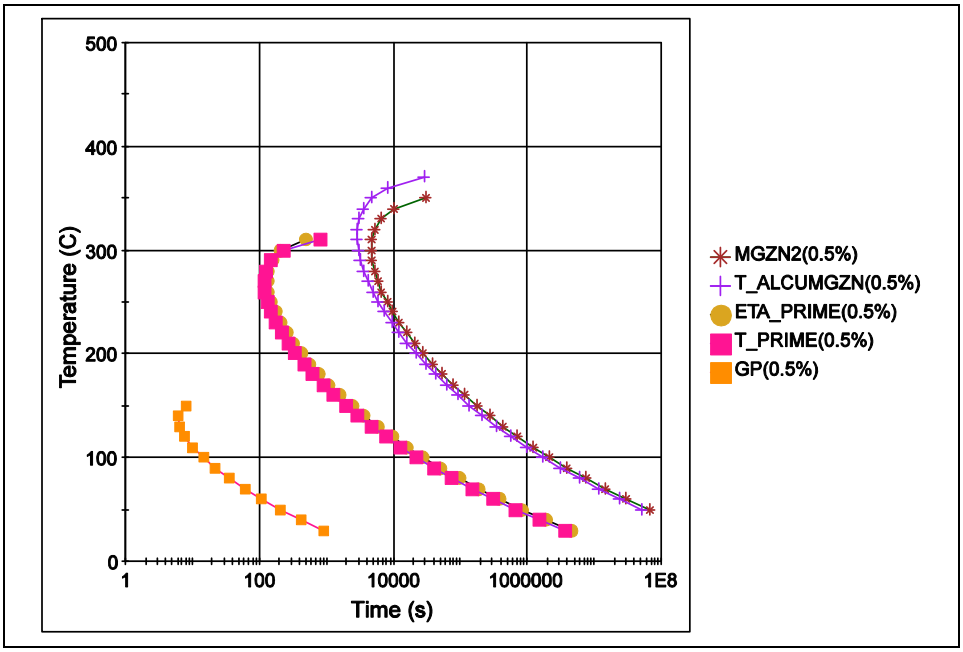

Figure 6. JMatPro calculated TTT curve for 7039 (start temperature = 500 °C).

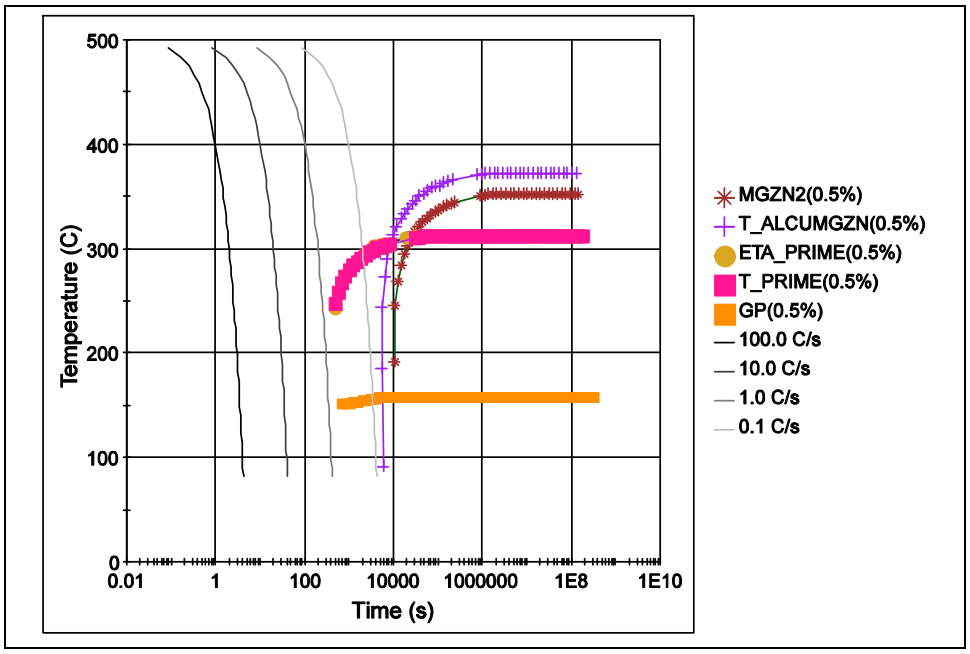

Figure 7. JMatPro calculated CCT curve for 7039 (start temperature = 500 °C).

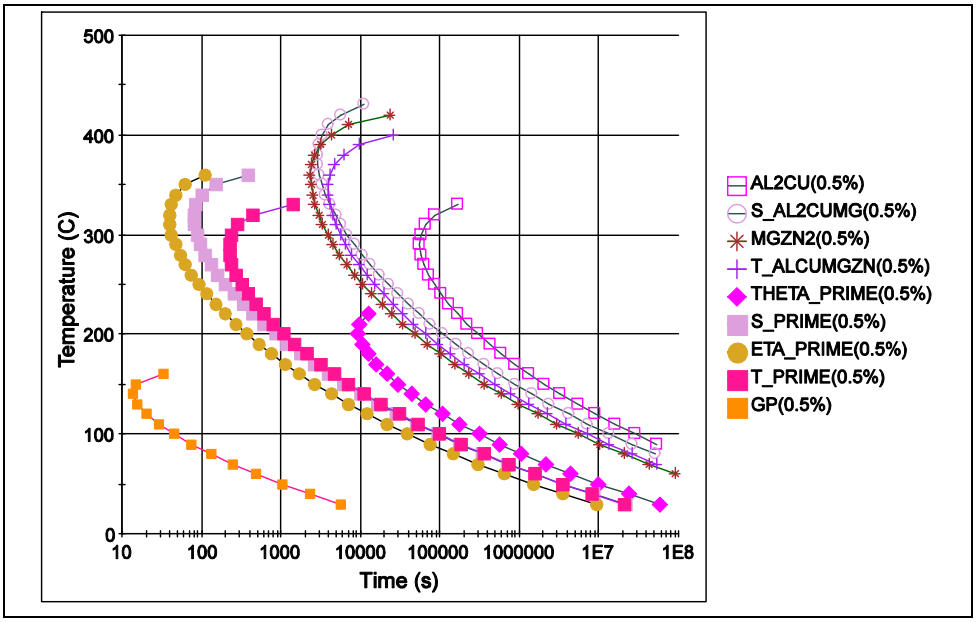

Figure 8. JMatPro calculated TTT curve for 7075 (start temperature = 475 °C).

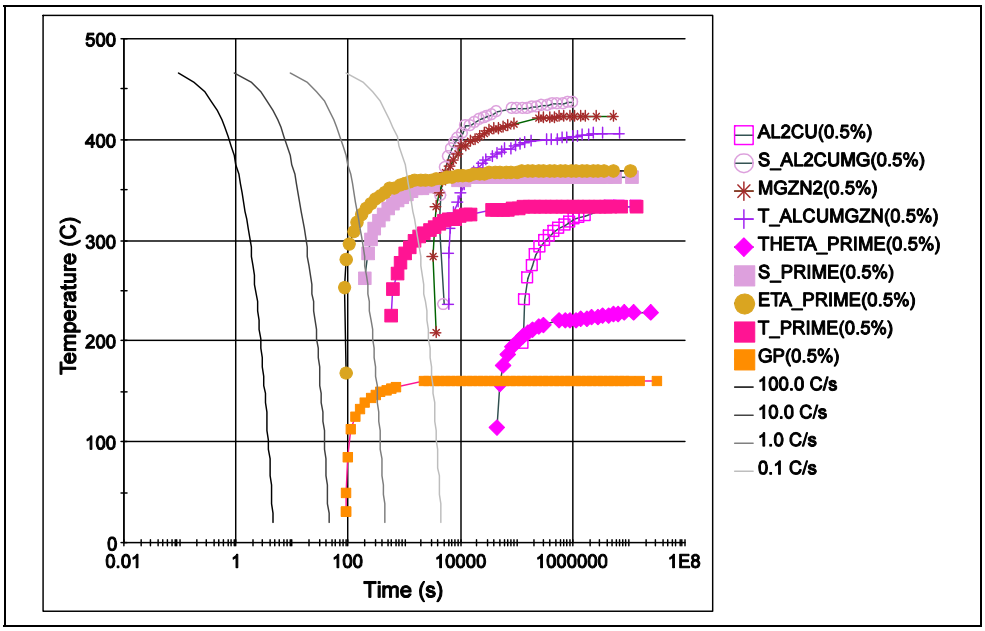

Figure 9. JMatPro calculated CCT curve for 7075 (start temperature = 475 °C).

3.3 JMatPro Calculated Temperature Step Calculations

3.3.1 Gibbs Partial Free Energy of Alloy Elemental Components

JMatPro TS plots (see figures 10–12) reveal the partial Gibbs energy as follows:

$$\bar{G} = \left(\frac{\delta G}{\delta n_i}\right)_{T,p,N_j,\ldots}, \tag{30}$$

where $\bar{G}$ is partial free energy of element i in the alloy or phase and δG is the change in the total free energy with the addition of a small amount of component i, δn_i, under conditions of constant temperature, pressure, and composition for elements j…≠ i. $\bar{G}$ alternatively is called the *chemical potential*, μ_i, of component i in the system or phase. The chemical potential is an important thermodynamic variable, as it describes how the free energy, the driving force for phase transformation of a given phase, will change when component atoms are added or removed. Activity and chemical potential are a measure of the tendency of the atom to leave solution or the phase. Cases for which $\bar{G}$ energies are negative are thermodynamic conditions where component solutions or mixtures tend to remain in solution or phase. Cases in which $\bar{G}$ energies are positive are conditions where components tend to leave solution to form their own phase (e.g., the phases of high-Si casting alloys or C precipitation in steels.) These Al-Zn-Mg 7XXX alloys demonstrate $\bar{G}$ energies for components that are more or less negative, consistent with their ability to form respective stable solutions and phases. The main elements of these Al 7XXX alloys, Zn and Mg, have relatively low or near aluminum-equilibrium $\bar{G}$ energy values with respect to the standard states for aluminum, implying that they readily form solutions (figures 10–12) but perhaps less in non-equilibrium weld conditions. The elements Cu and Si in

7XXX alloys have $\bar{G}$ energies that are significantly more negative than aluminum, suggesting that these elements may tend to form both aluminum-7XXX alloy solutions and phases, and that a uniform solid solution may be somewhat more difficult to achieve with non-isothermal practices of casting and fusion welding. Near ambient temperature for 7020, it is shown that the elements have increasing negative $\bar{G}$ in order of Zn, Mg, Si, Cu, Mn, Cr, Fe, Ti, Zr, and Ni.

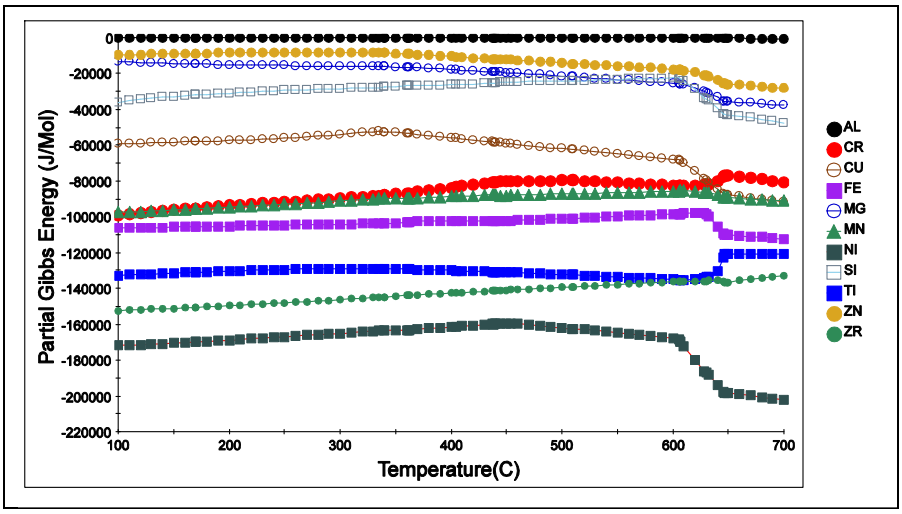

Figure 10. Partial Gibbs energy for alloy 7020 component elements, with Al at standard state.

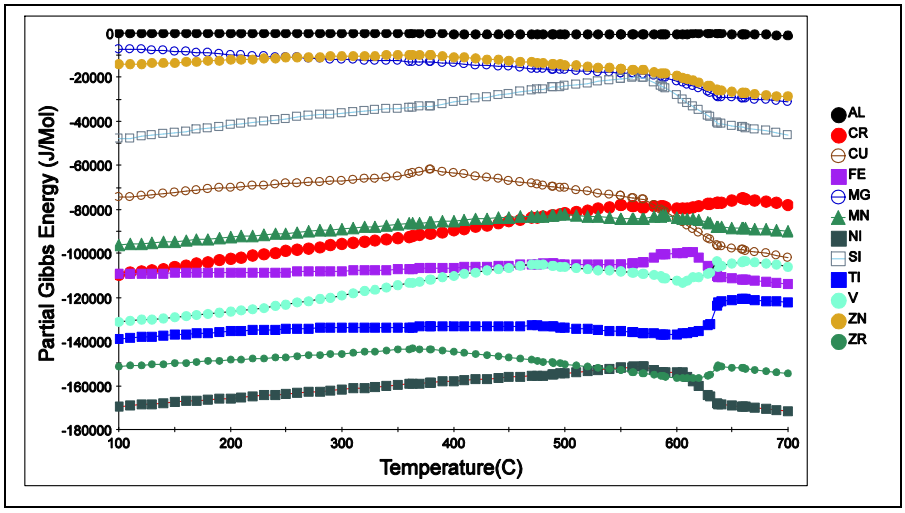

Figure 11. Partial Gibbs energy for alloy 7039 component elements, with Al at standard state.

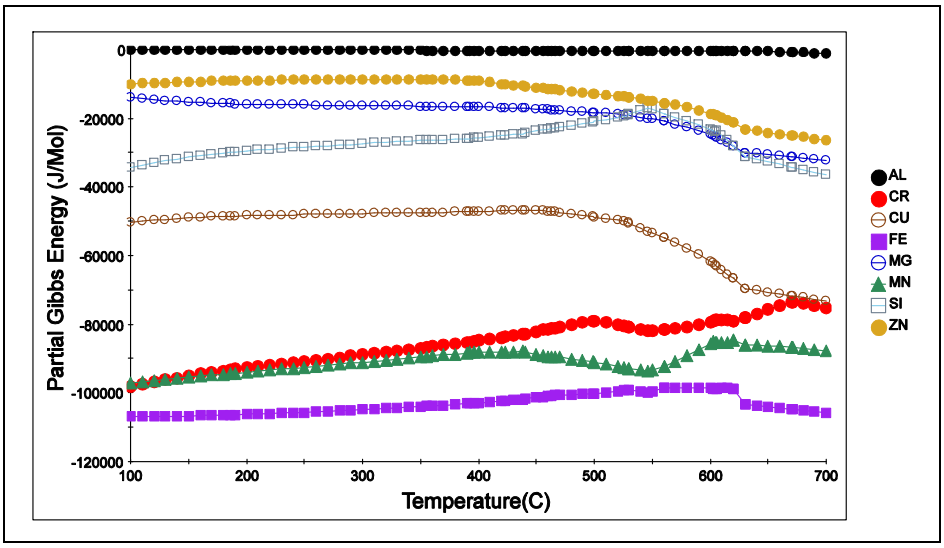

Figure 12. Partial Gibbs energy for alloy 7075 component elements, with Al at standard state.

Since these alloys are all 7XXX alloys, the plots are similar, but there are also subtle differences in how partial Gibbs energies change with temperature, first during the transformation of liquid to solid phases, and secondly over the temperature interval of the solid phases from higher to lower temperatures. Over the temperature range of liquid to complete solidification, the 7020 elements Ti, Zr, and Cr reveal increasingly more negative values of $\bar{G}$, and the Zn, Mg, Si, Cu, and Fe reveal less negative $\bar{G}$. Over the temperature range from high temperature solid to near ambient temperature, alloy 7020 reveals near constant $\bar{G}$ for Ti and Fe; increasingly negative $\bar{G}$ for Zr, Mn, Cr, and Si; and trends of less negative to constant $\bar{G}$ for Zn and Mg. The 7039 alloy reveals trends for Cu, Mn, Cr, V, and Ni elements with more significant increasingly negative $\bar{G}$ over the interval of high to low temperatures of the solid. Unlike the 7020 or 7075 alloys, there is a trend of less negative $\bar{G}$ for Mg in 7039 near age and ambient temperatures that suggests a lesser tendency to form a solution. The most extremely negative $\bar{G}$ of the Mn, Fe, V, Ti, Zr, and Ni components suggest these elements are likely not to form significant concentration levels of solid solutions that may be amendable to solid solution quench and hardening, but they may instead be more prone to forming stable inclusion phases.

3.3.2 Activities and Activity Coefficients of Alloy Elemental Components

JMatPro plots (see figures 13–15) and tabulated values (see table 6) describe observable levels of the activities, a_i, of the elemental components in 7020, 7039, and 7075. The actual mole fractions, X_i, of the alloy components (see table 7) may be used to estimate activity coefficients (see table 8). If a_i is low, atoms are highly stable in solution. Levels of a_i in plots may be developed from ΔG_{mix} curves (*7*, *9*). Al has the greatest values of a_i, consistent with its role as the major constituent phase. The plots and tabulated activities of selected components reveal that other than the Al solute, Zn has its maximum levels of 0.20 a_{Zn} around solvus temperatures

for the $MgZn_2$ phase at 334.9° and 392.7° C for Al-Zn-Mg 7020 and 7075 and 0.16 a_{Zn} for the T phase in 7039 at 379.4° C, respectively (see figures 3 and 13–15 and tables 6 and 8). However, Zn has significantly less activity in solution either at 100° C or at 650° C in the liquid state. Following Al and Zn, Mg has the next highest levels of a_i, with a maximum 0.104-a_{Mg} level in 7039 at 100° C, which is the highest a_i at this temperature for any alloy. Following Mg, Si has 0.046, 0.056, and 0.083 a_i levels, respectively, for 7020, 7039, and 7075 at or near the solidus temperatures of 605.4°, 570.3°, and 546.5° C (see table A1 in the appendix).

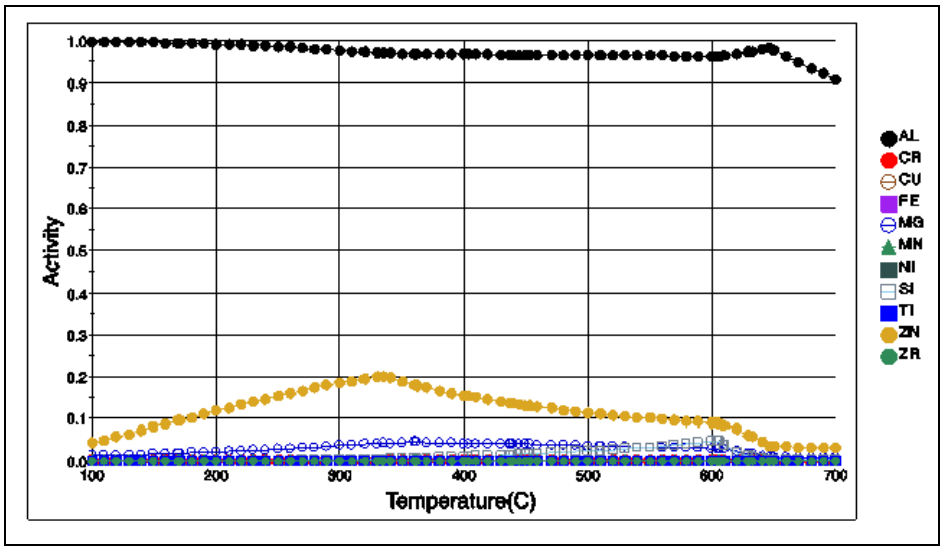

Figure 13. Activity values for alloy 7020 component elements.

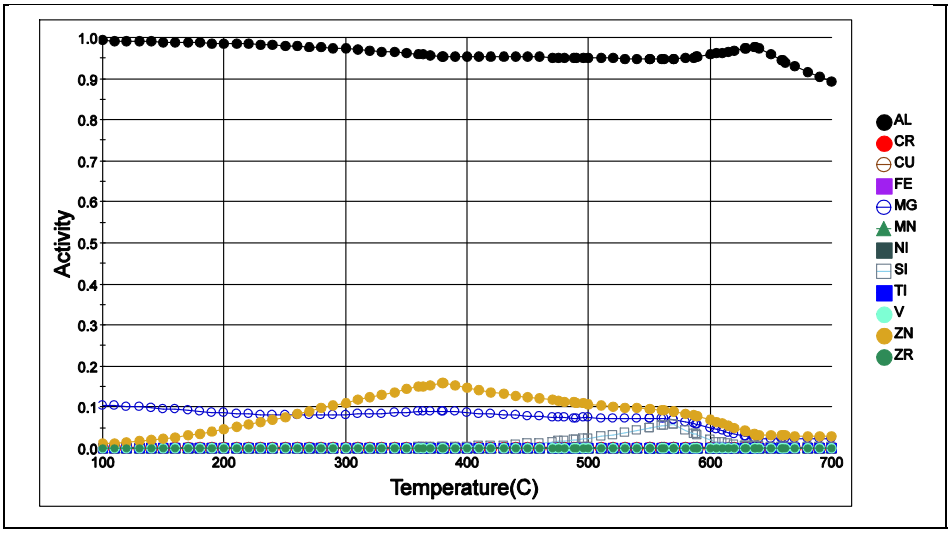

Figure 14. Activity values for alloy 7039 component elements.

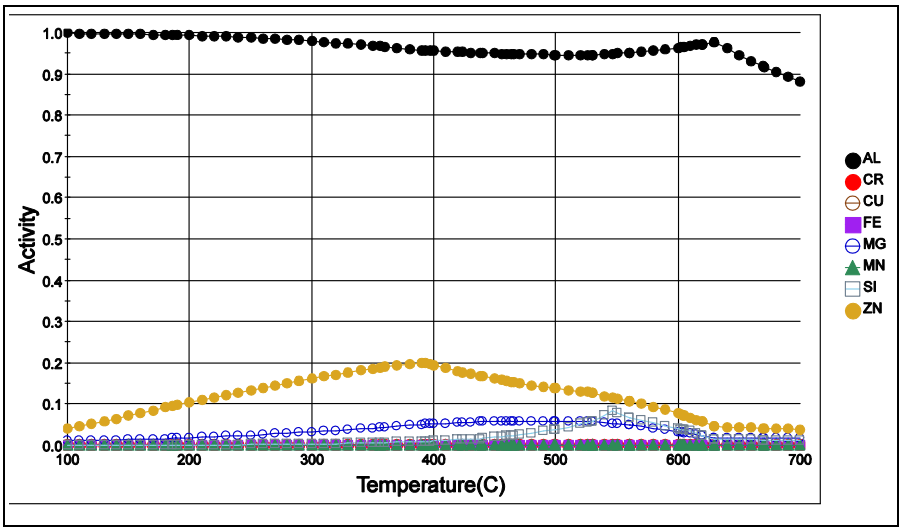

Figure 15. Activity values for alloy 7075 component elements.

Table 6. Selected values of JMatPro calculated activity, a_i.

Alloy	Temp. (C°)	Component					
		Al	Si	Cu	Mg	Cr	Zn
7020	100.0	0.9984	0.0000	0.0000	0.0146	0.0000	0.0435
	160.0	0.9956	0.0001	0.0000	0.0172	0.0000	0.0872
	334.9	0.9698	0.0042	0.0000	0.0425	0.0000	0.2003
	480.0	0.9654	0.0204	0.0001	0.0372	0.0000	0.1197
	650.0	0.9616	0.0035	0.0000	0.0095	0.0000	0.0338
7039	100.0	0.9929	0.0000	0.0000	0.1037	0.0000	0.0101
	160.0	0.9890	0.0000	0.0000	0.0939	0.0000	0.0266
	379.4	0.9543	0.0022	0.0000	0.0909	0.0000	0.1579
	480.0	0.9514	0.0207	0.0000	0.0737	0.0000	0.1109
	650.0	0.9582	0.0042	0.0000	0.0218	0.0001	0.0318
7075	100.0	0.9986	0.0000	0.0000	0.0112	0.0000	0.0395
	160.0	0.9962	0.0002	0.0000	0.0139	0.0000	0.0777
	392.7	0.9569	0.0092	0.0002	0.0509	0.0000	0.2008
	480.0	0.9467	0.0337	0.0005	0.0577	0.0000	0.1417
	650.0	0.9463	0.0142	0.0001	0.0184	0.0001	0.0430

Table 7. Mole fraction of components X_i, the composition by atomic percent (a%).

Alloy	Al	Si	Fe	Cu	Mn	Mg	Cr	Zn	Ti	Zr	Ni	V
7020	0.9610	0.0010	0.0013	0.0007	0.0013	0.0142	0.0009	0.0190	0.0002	0.0004	0.0000	0.0000
7039	0.9432	0.0013	0.0010	0.0002	0.0012	0.0327	0.0010	0.0180	0.0001	0.0000	0.0011	0.0001
7075	0.9303	0.0040	0.0025	0.0071	0.0015	0.0291	0.0012	0.0242	—	—	—	—

Table 8. Estimated value of activity coefficient $\gamma_i = a_i/X_i$.

Alloy	Temp. (°C)	Component					
		Al	Si	Cu	Mg	Cr	Zn
7020	100.0	1.04	0.01	0.00	1.03	0.00	2.29
	160.0	1.04	0.13	0.00	1.21	0.00	4.59
	334.9	1.01	4.19	0.05	2.99	0.00	10.53
	480.0	1.00	20.61	0.09	2.62	0.00	6.29
	650.0	1.00	3.50	0.02	0.67	0.05	1.77
7039	100.0	1.05	0.00	0.00	3.17	0.00	0.56
	160.0	1.05	0.00	0.00	2.87	0.00	1.48
	379.4	1.01	1.75	0.05	2.78	0.00	8.77
	480.0	1.01	16.15	0.08	2.25	0.00	6.16
	650.0	1.02	3.31	0.01	0.67	0.05	1.76
7075	100.0	1.07	0.00	0.00	0.39	0.00	1.64
	160.0	1.07	0.05	0.00	0.48	0.00	3.21
	392.7	1.03	2.28	0.03	1.75	0.00	8.30
	480.0	1.02	8.39	0.07	1.99	0.00	5.86
	650.0	1.02	3.52	0.01	0.63	0.04	1.78

Mole fractions of alloy components (see table 7) are a means to compare deviations of the a_i levels from ideal solution behavior for which $a_i \cong X_i$, and estimates of activity coefficients $\gamma = a_i/X_i$ at 100, 160, 334.9–392.7, 480–490, and 650 °C (liquid) (see table 8) reveal the deviation of the component activities from ideal solution behavior. It is shown that Al has a_{Al} values that are slightly $>X_{Al}$, with slight positive deviations of γ. The liquid phase of each alloy at 650 °C has activity coefficients with negative deviation, with exception to Si, Zn, and Al. Si has the greatest positive γ deviation of all components for the 480° C and liquid conditions but negative deviation for medium and low temperatures. Following Si, Zn has the second greatest positive γ deviation at η and T phase solvus temperatures near 334.9–392.7 °C (see table A1 in the appendix). Following Zn, the Mg activity coefficients have positive deviation for the 100, 160, 334.9–392.7, and 480 °C for 7020 and 7039 but negative deviation for 7075 at 100 and 160 °C. At low temperatures, the activity coefficient of Mg in 7039 is the greatest in magnitude and has

the greatest positive deviation. The Cu activity coefficients have negative deviation. At 100°, Zn appears to have a moderate positive deviation from ideality in the 7020 alloy; however, at this same temperature, Mg has significantly greater positive deviation in the 7039 alloy.

Following certain fusion weld procedures in Al-Zn-Mg-(Cu) alloys, a condition known as "white zones" may occur that results in the presence of Zn in solution in the grain boundaries, a situation deleterious to SCC (*20*, *33*). It appears that the high a_{Zn} values of Zn may contribute to white zones from the liquation of Zn containing hardening precipitates or the solute rejection of the matrix during non-isothermal temperature excursions of weld processes through temperatures of 334.9–392.7 °C. Slow cooling rates of weld metal have been proposed to minimize the thickness of the white zones (*33*). It has also been shown that maintaining solute Zn atom in grain boundaries at low concentrations is greatly beneficial for enhancing resistance to SCC (*33*).

3.3.3 Liquid Phase Compositions Over the Interval of Liquidus to Solidus Temperatures

Figures 16–18 reveal JMatPro calculated elemental compositions of liquid for 7020, 7039, and 7075 aluminum calculated under TS equilibrium conditions. Scheil-Gulliver solidification (*2–5*, *7*) assumes conditions of stepwise complete liquid mixing and no diffusion in the solid, eutectic solidification (see equation 29) that results in solid phases becoming lean in solute in the center of the dendrite, with the liquid becoming more enriched in solute as solidification proceeds. The JMatPro TS calculations predict that Si and Cu partition greatly to eutectic liquid (see table 9). Alloy 7020 reveals less partitioning of solutes to liquid eutectic phase, with exception of Si. Alloy elements Cu, Fe, Mg, Mn, Ni, Si, and Zn solidify as eutectic (see equation 11) so that the center of dendrites will contain less solute than outer layers that solidify at lower temperatures. Alloy elements Cr, Ti, and Zr solidify via a peritectic (*7*, *12*) reaction as follows:

$$L + \alpha = \beta. \tag{31}$$

In this reaction, the last stage to solidify may contain less solute than an intermediate stage of solidification. It may be seen that the more highly alloyed 7039 and 7075 compositions are predicted to become highly enriched with solute and constituent phase elements during solidification and thereby have greater risk for segregation of alloy elements during the solidification process either in casting or welding, which may have deleterious consequences to mechanical properties of strength and ductility.

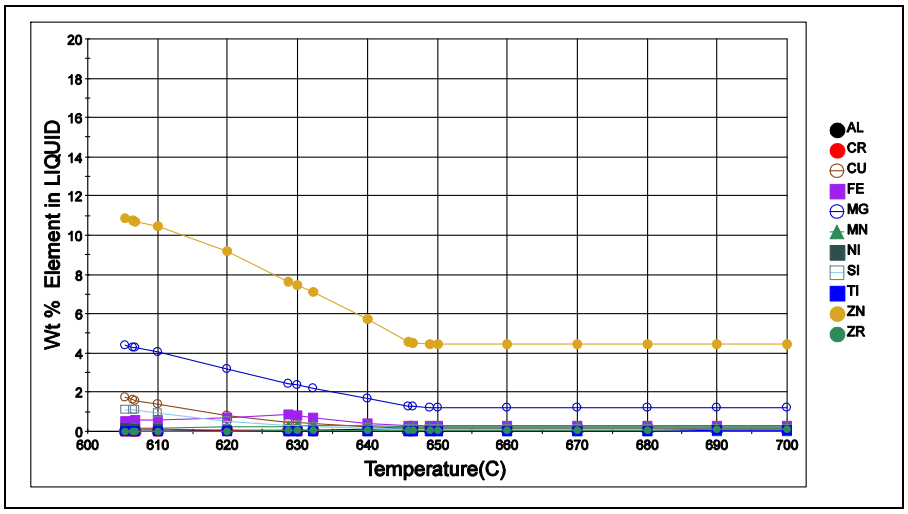

Figure 16. JMatPro calculated weight-percent of elemental composition of the liquid phase in 7020.

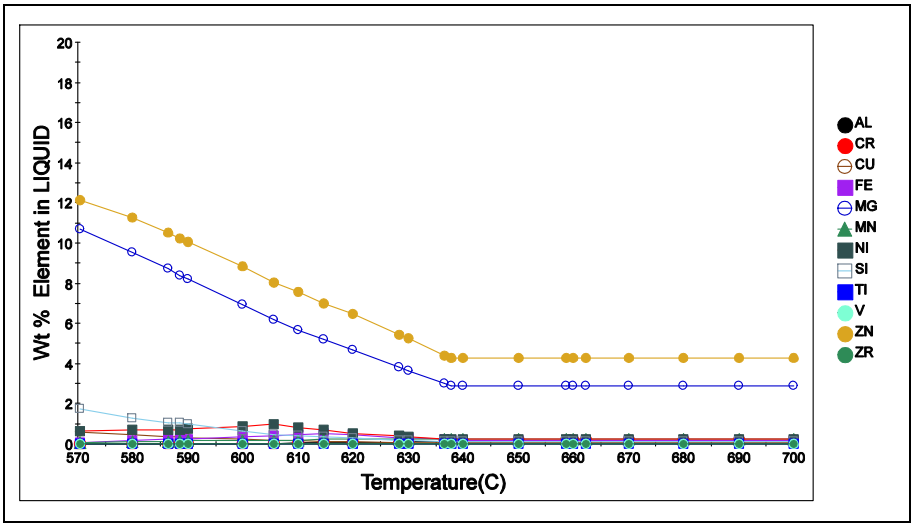

Figure 17. JMatPro calculated weight-percent of elemental composition of the liquid phase in 7039.

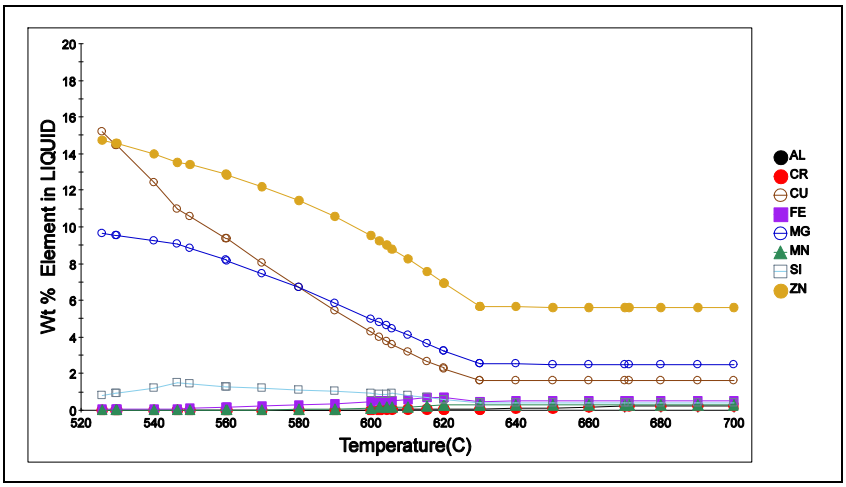

Figure 18. JMatPro calculated weight-percent of elemental composition of the liquid phase in 7075.

Table 9. JMatProTS elemental compositions of liquid.

Alloy	Liquid at ~ T Solidus (S)				Liquid at T Liquidus (L)				Composition S/L			
	Si	Zn	Mg	Cu	Si	Zn	Mg	Cu	Si	Zn	Mg	Cu
T(°C)	Composition (Weight-Percent)				Composition (Weight-Percent)				Composition Ratio			
7020	1.2	11	4.3	1.8	0.10	4.47	1.24	0.16	12.0	2.5	3.5	11.3
7039	1.9	12.1	10.8	0.6	0.13	3.8	2.87	0.05	14.6	3.2	3.8	12.0
7075	0.90	14.8	9.8	15.2	0.40	5.6	2.5	1.6	2.3	2.6	3.9	9.5

3.3.4 H, S, and G Plot Details

The enthalpies for 7020 over the temperature range of 100–700 °C (see figure 19) reveal negative H values for all phase components, with exception to the Al phase for which the H values are positive as an endothermic reaction. Exothermic mixing indicates a release of heat energy and a tendency toward ordering and compound formation between components such that attractions between unlike atoms are greater than those of similar or like atoms. Endothermic mixing or reactions have a tendency toward phase separation or clustering such that attractions of like atoms are greater than the dissimilar ones. The standard state of components for H is taken at 298 K = 25 °C for which H = 0. The $(\delta H/\delta T)_P$ slopes of each phase are linear and are the individual C_p values of the phases (see equation 5). The ΔH values may be obtained by the summation of the area under the curves of C_p vs. T (see equation 6). It may be observed that the Al_3M, Al_3Fe, Al_9M_2, and Mg_2Si phases likely have characteristics of compounds with strong atomic bonds. There are large phase-to-phase variations in the H magnitudes of the 7070 Al phase components, consistent with changes in bond energy and lattice strain or volume change, and there is a distinct increase in H from the solid phases to the Al liquid phase.

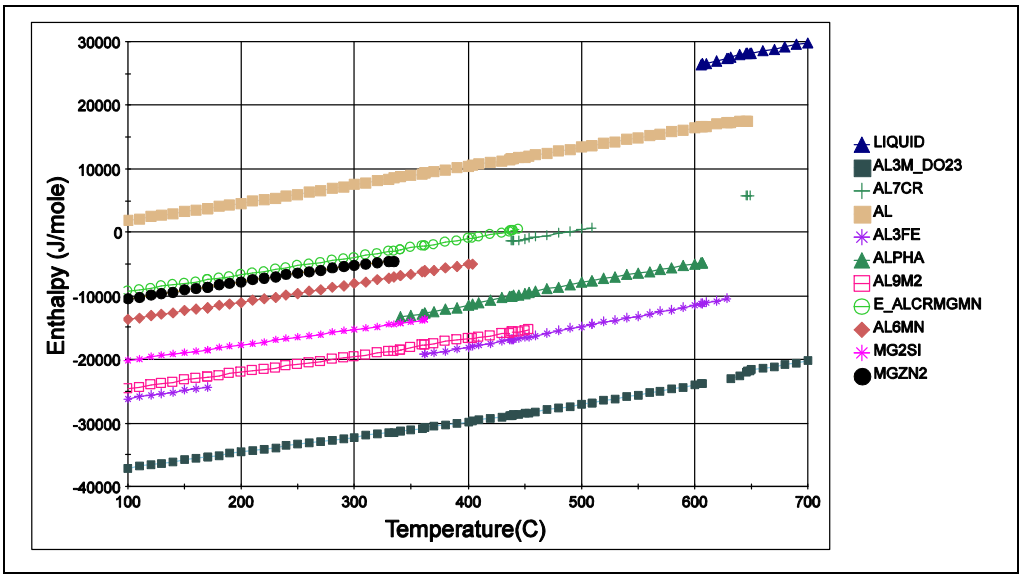

Figure 19. JMatPro TS calculated of H (J/mole) for 7020 equilibrium phases.

The JMatPro entropy plot (see figure 20) reveals S value phase details of the 7020 in J/mole-K. The ΔS values are the area of Cp/T vs. T or Cp vs. ln T evaluated over a T range (see equation 8). The S values reveal distinct changes of increasing S in changes from the solid to the liquid Al phase. A slight negative deviation curvature of S with increasing T is present. The $MgZn_2$, Al, and liquid phases reveal high S values.

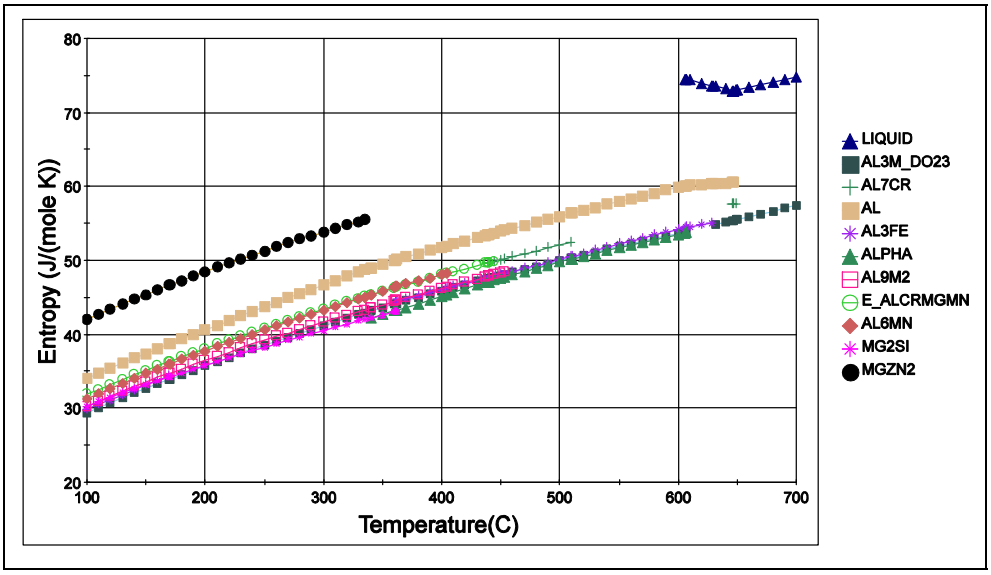

Figure 20. JMatPro TS calculated of S (J/mole-K) for 7020 equilibrium phases.

A plot of JMatPro calculated Gibbs free energy G = H – TS (see equation 1) of 7020 alloy phases (see figure 21) reveals Gibbs energy of equilibrium phases over the temperature range of 100–700 °C. For G, H is dominant at low temperatures and S at high temperatures.

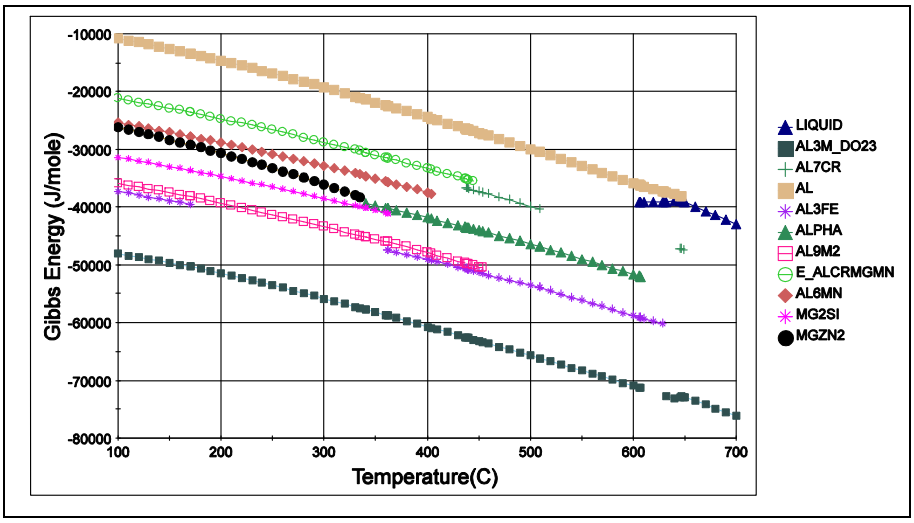

Figure 21. JMatPro TS plot of G (J/mole) values for equilibrium phases in 7020.

If a system is closed with constant P and components, then from equation 19, the slope of a G vs. T plot is $\left(\frac{\delta G}{GT}\right)_P$ = –S (see equations 14, and A2). The curvature is $\left(\frac{\delta^2 G}{\delta T^2}\right)_P$ = –C_p/T (see equations 7 and A6 in the appendix).

The plots of phases with lower values of G have greater stability. It may be assumed that a significant portion of the phases are formed during solidification and cooling, and the objectives of processing therefore include optimization and refinement of the phase structure on the microscale by heat treatments using solution treatments for phase dissolution, quenching to retain desired matrix microstructures at low ambient temperature, and then aging for precipitate hardening. At ambient temperature, reactions either do not or slowly occur. It may be seen that with respect to Gibbs energy and Mg, the Mg_2Si is strongly preferred, and the E AlCrMgMn phase is preferred in free energy over the hardening metastable phase that progresses to $MgZn_2$, potentially resulting in a loss of strength in case of inappropriate solution treatment. Similarly, the impurity element Cr and Mn elements that are present in AlCrMgMn and AlFeMn are Mg-competitors to the $MgZn_2$ for the 7020 composition. Therefore, under some conditions of processing, Cr and Mn-containing precipitates may have some deleterious effects that lower strength rather than mitigate corrosion or control grain recrystallization or the morphology of Fe-based constituent phases (*16–19*).

3.3.5 Equilibrium Phases and Precipitates

Details of TS plots (see figures 22–24) for weight-percent of equilibrium phases over the temperature intervals from liquid at 700–100 °C for 7020, 7039, and 7075 reveal the transformational relationships and amounts of the equilibrium constituent phases precipitated. The plots predict that the 7020 alloy responds well to solution treatment, typically 480 °C, by significantly dissolving both the hardening evolved precipitates and other constituent phases. It may be seen that the 7020 phase transformation relationships are somewhat similar to those of

3104 (see figure 1) for $Al_6(FeMn)$ intermetallic phase and α AlFeMnSi. Together, the 7020 CCT and TTT diagrams and weight-percent phase TS plots reveal that a 7020 solution treatment at high temperature (480 °C) followed by a quench to ambient temperature is effective in reducing the amount and size scale of potential deleterious phases and efficiently providing Mg and Zn solute for precipitation hardening at a fine scale. In contrast, the 7039 and 7075 alloys retain greater amounts of hardening phases and microconstituents at solution treatment temperatures and at temperatures either for end quench or age hardening. It may also be seen that significant amounts of constituent phases in 7039 and 7075 persist near and up to temperatures of the liquid phase, so that care in solution treatments is required to avoid deleterious effects of localized melting and liquation from the inherited eutectic solidification segregated regions of microstructure that have low liquidus temperatures. With appropriate magnitude and state of tensile or shear stress or strain, microconstituent particles in materials are potentially deleterious when they act to nucleate voids or microcracks, respectively, that may grow and coalesce to promote fracture and shear instability or lower fatigue life (*29*, *30*). Tables A1–A3 in the appendix list the JMatPro TS calculated weight-percents of 7020, 7039, and 7075 phases. Microstructures of 7020-T651 and 7075 (see figures A1–A3 in the appendix) reveal precipitates of constituent phases, and table A4 in the appendix provides the experimentally determined chemical compositions of the alloys and their microstructures.

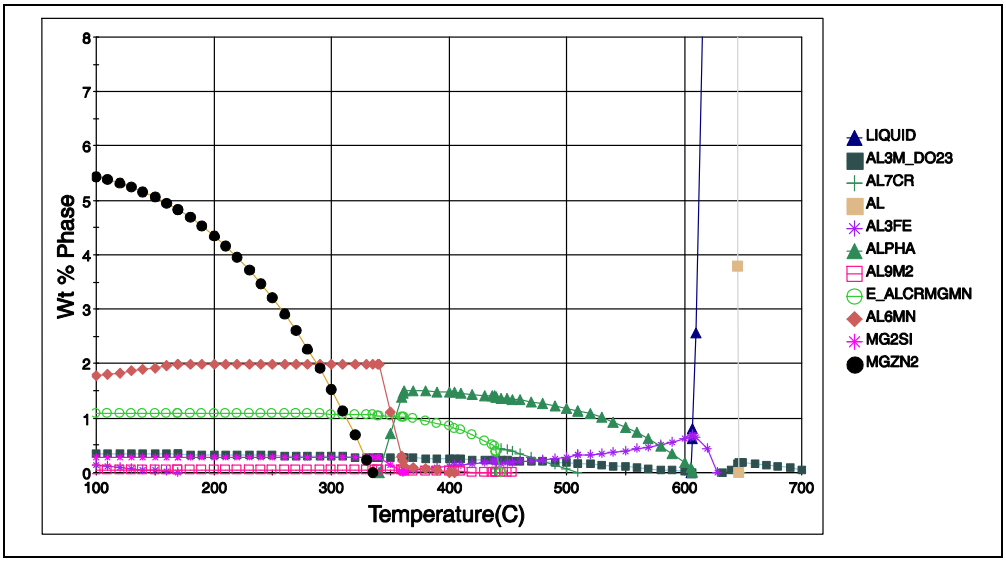

Figure 22. Section of JMatPro TS plot for weight-percent of 7020 equilibrium phases.

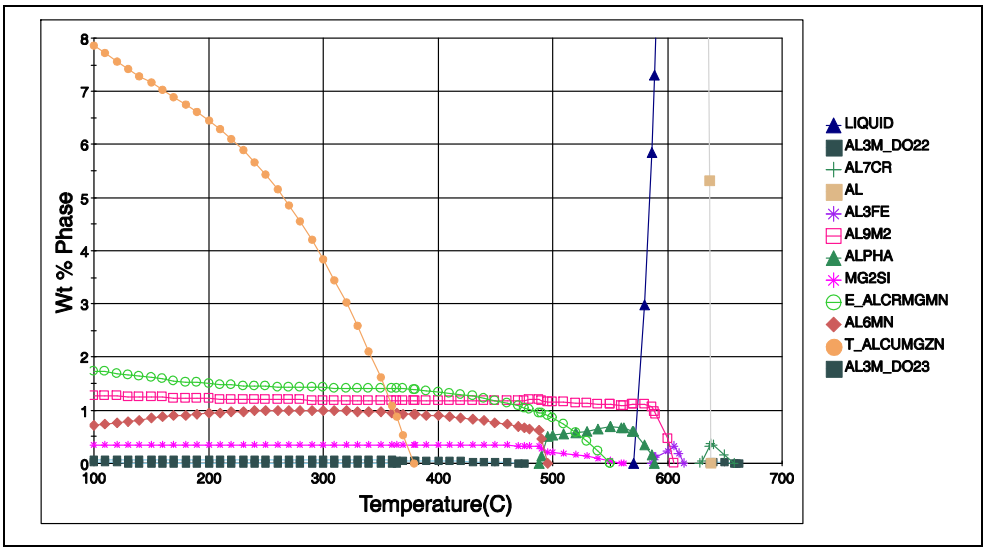

Figure 23. Section of JMatPro TS plot for weight-percent of 7039 equilibrium phases.

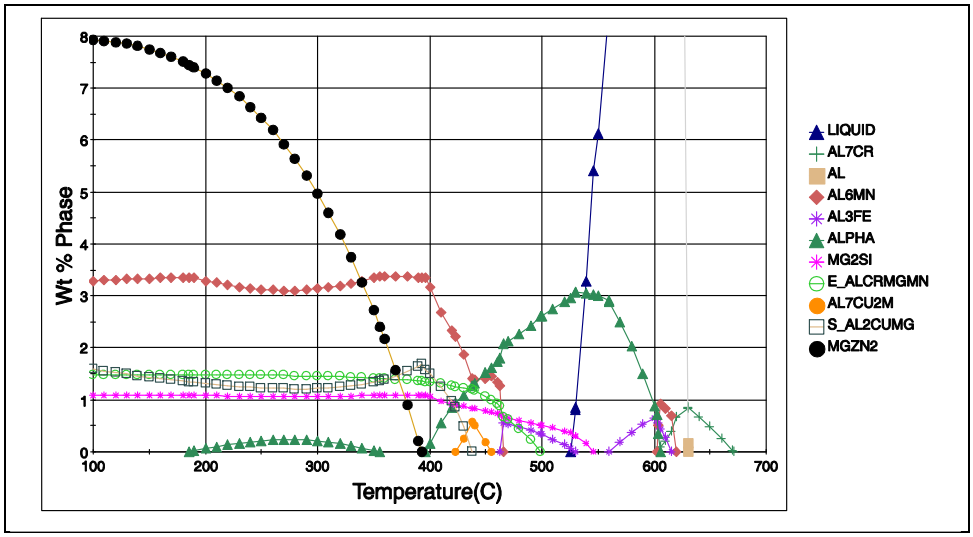

Figure 24. Section view of JMatPro TS plot for weight-percent of 7075 equilibrium phases.

From inspection of JMatPro TS weight-percent phase plots (see figures 22–24), the ideal temperatures for solution treatment where maximum solubility is obtained appear to be 475–480 °C for 7020, 480 °C for 7039, and 450–490 °C for 7075. Alloy 7020 appears to demonstrate significant advantages over 7039 and 7075 alloys in capability for solution treatment (see table 10). It may seen by JMatPro point coordinate readouts or plot inspection that alloy 7020 has a low fraction of constituent phases, may be solution treated at high temperature, and retains ~98.08% Al or 1.92% of constituent phases at a solution treat temperature of 480 °C. However, 7039 retains 96.98% Al or 3.02% of phase constituents, and 7075 is calculated to retain 96.37% of Al or 3.63% of phase constituents at 490 °C.

Table 10. Constituent weight-percent of equilibrium phases near solution heat treatment temperatures.

Alloy	Temp. (°C)	Al (%)	α AlFeMnSi (%)	Al_9M_2 (%)	Mg_2Si (%)	Al_3Fe (%)	Al_7Cr (%)	Al_3M DO23 (%)	Al_6Mn (%)	E AlCrMgMn (%)
7020	480	98.08	1.27	—	—	0.24	0.22	0.20	—	—
7075	490	96.37	2.42	—	0.56	0.42	—	—	—	0.22
7039	490	96.98	0.13	1.19	0.29	—	—	—	0.47	0.94

JMatPro calculated weight-percents of phases are shown at typical age hardening temperatures of these alloys approximate to 160 °C after quenching from 500 °C (see figures 25–27 and table 11). It may be seen that 7020 with 91.34 weight-percent Al phase has significantly less equilibrium phase constituent contents than either 88.7 weight-percent Al 7039 or 84.99 weight-percent Al 7075. Given eutectic solidification structures and the limitations of time-temperature on solute dissolution, in practice, it may be more likely that the computed predictions of JMatPro equilibrium phase contents may be obtained at high temperatures of industrial solution treatment with the 7020 alloy that has low segregation and solute content.

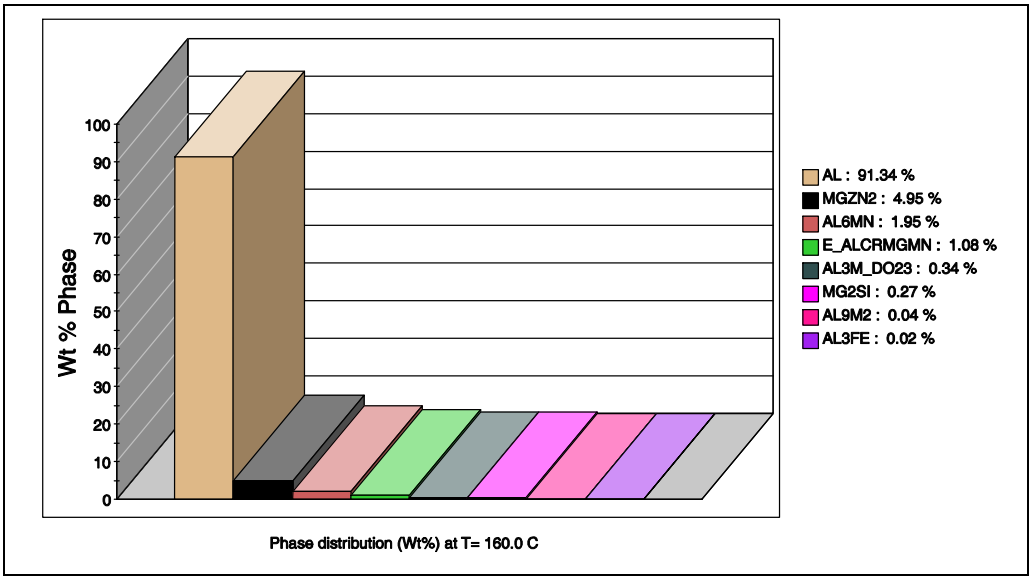

Figure 25. JMatPro TS phase distribution plot for 7020 at 160 °C.

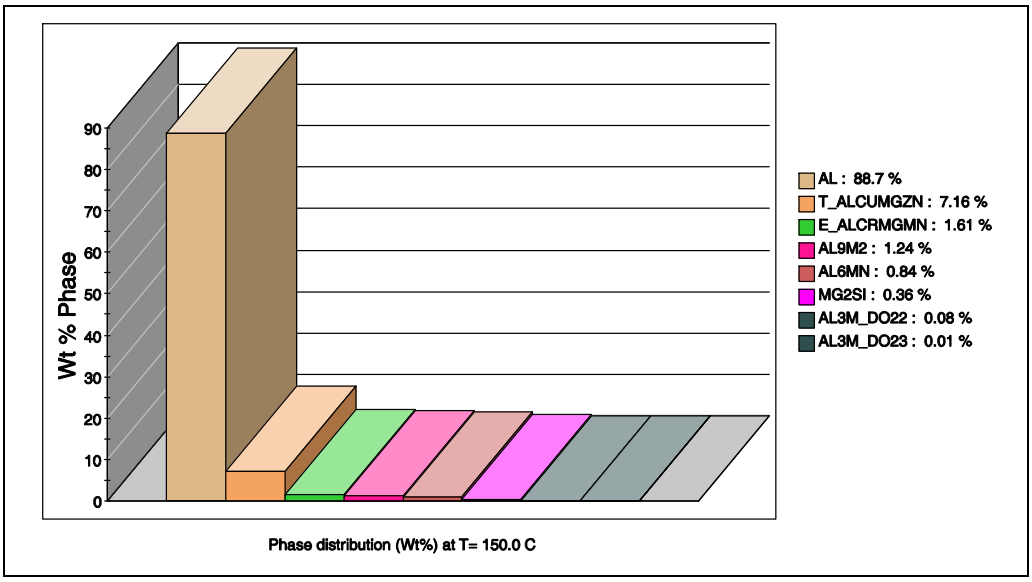

Figure 26. JMatPro TS phase distribution plot for 7039 at 150 °C.

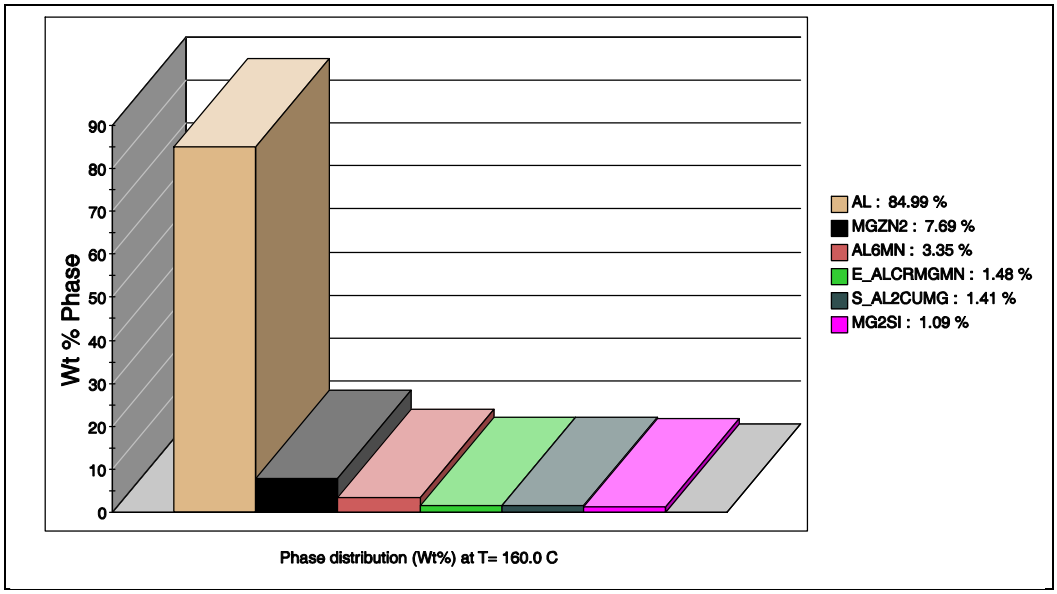

Figure 27. JMatPro TS phase distribution plot for 7075 at 160 °C.

Table 11. Constituent weight-percents of equilibrium phases near precipitation hardening temperatures.

Alloy	Temp. (°C)	Al (%)	$MgZn_2$ (%)	α AlFeMnSi (%)	Al_9M_2 (%)	Mg_2Si (%)	Al_3Fe (%)	Al_7Cr (%)	Al_3M DO23 (%)	Al_6Mn (%)	E AlCrMgMn (%)
7020	160	91.34	4.95	—	0.04	0.27	0.02	—	0.34	1.95	1.08
7075	160	84.99	7.69 Al_2CuMg 1.41	—	—	1.09	—	—	— DO22 —	3.35	1.48
7039	150	88.70	— AlCuMgZn 7.16	—	1.24	0.36	—	—	0.08 DO23 0.01	0.84	1.61

3.3.6 JMatPro Temperature Step Calculations of Cu Content of η Phase

Stress corrosion concerns of the 7XXX alloys have been largely solved by multiple approaches. Material designs may restrict total alloy content and thereby the quench rate requirements and the levels of strength, all of which lessen stress incompatibilities in the microstructure and propagation sensitivity to crack size. Chemistries in the high-Zn, low-Mg η phase alloys are less temperature sensitive to overage effects, less sensitive to onset of deleterious microstructure during quench processing, and also allow slow quench processing and low residual stress (see figures 4 and 5). Duplex T6 and overage T7 heat treatments mitigate effects of the hydrogen grain boundary embrittlement mechanism (*12*, *19*, *21*). To further improve resistance to SCC in weldable structural Al-Zn-Mg alloys, Zr is microalloyed to control recrystallization and grain shape during hot work and microalloying, and Cu of <0.20 weight-percent is used to enhance effectiveness of the duplex T6 or T7 tempers in resisting SCC without any deleterious mechanical effect on weldment properties from effects of eutectic segregation following welding. Holroyd and Hardie (*21*) have demonstrated that Cu microalloyed materials 7020 and 7018 with T7651 tempers can be highly effective in improving resistance to SCC; however, there have been concerns of SCC in high-strength 7039 alloys (*24*).

JMatPro calculations of Cu contents following solution treatment and precipitation aging (see figures 28–30) reveal Cu contents evolved from the hardening phases for 7020, 7039, and 7075 alloys are 3.2%, 0.7%, and 11%, respectively. By comparing these 7020 and 7039 plots, it may be seen that only small, <0.20-weight-percent additions of Cu are required to enhance the $MgZn_2$ Cu content. It may be seen that the JMatPro calculated values of Cu increase with temperature, and Hatch (*12*) makes note that x-ray analysis and electrical potential measurements reveal that Cu and Al more easily substitute for Zn in η with increasing temperatures.

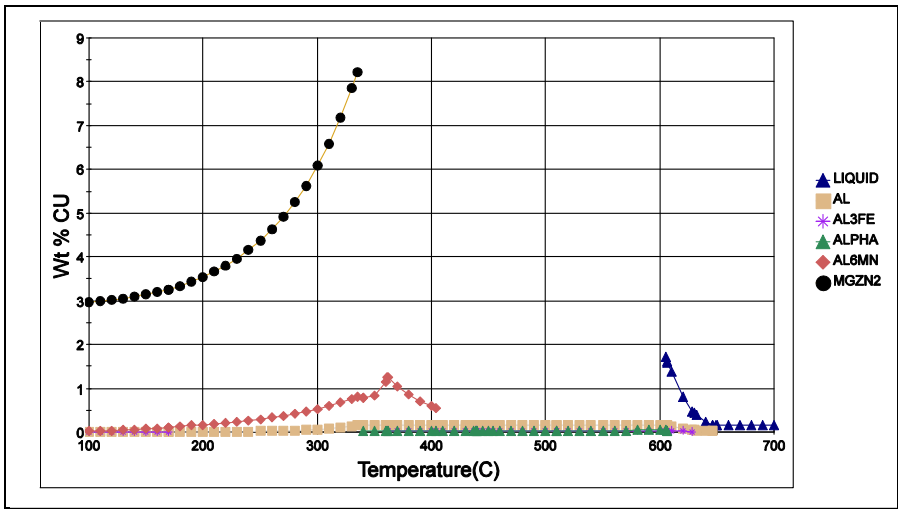

Figure 28. JMatPro calculated weight-percent of Cu for alloy 7020 phases.

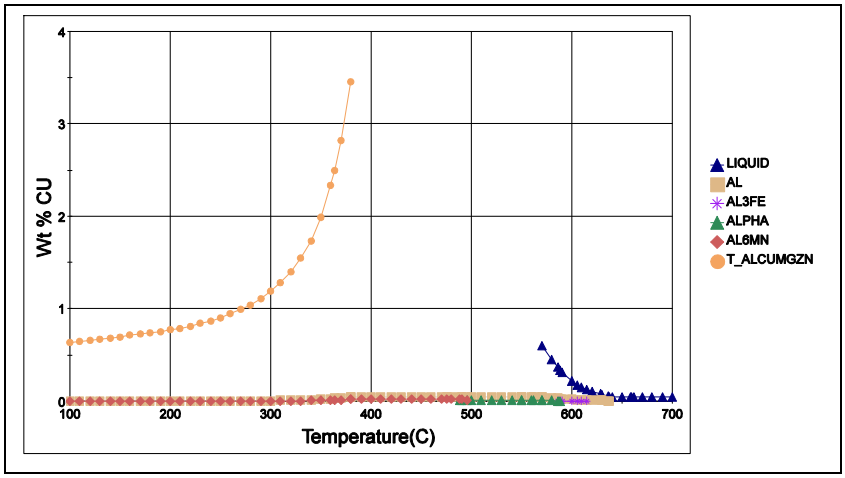

Figure 29. JMatPro calculated weight-percent of Cu for alloy 7039 phases.

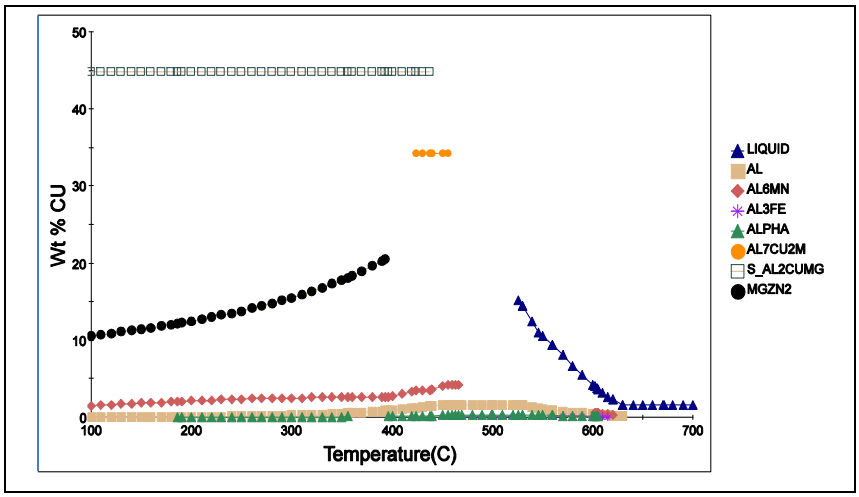

Figure 30. JMatPro calculated weight-percent of Cu for alloy 7075 phases.

3.3.7 JMatPro Weight-Percent Elements: α AlFeMnSi, Al_6Mn, E AlCrMgMn, ή, and $MgZn_2$ Phases

The JMatPro calculated elemental composition of the α AlFeMnSi, Al_6Mn, and E AlCrMgMn, $MgZn_2$, and ή phases in 7020 and 7075 are shown with TS plots of weight-percent element vs. equilibrium temperature (see figures 31–39). Since these 7020 and 7075 materials are used in the solution-treated and aged condition, the accuracy of the JMatPro calculated values may not in all cases predict the phases obtained by non-equilibrium experimental or industrial processes. However, in solution-treated and aged materials, the phases with elements of low-diffusivity Mn, Cr, and Fe may be expected to form or retain phases at solution treatment temperatures, or it is possible to form phases with these elements during the time interval of quenching from solution treatment and then retain these secondary phases at ambient temperature or to react the phases at solution treatment temperatures (see figures 22–24 and table 10). Inspection of the JMatPro weight-percent element of phase plots (see figures 31–39) reveals near-identical 7020 and 7075 chemistries for the α AlFeMnSi and E AlCrMgMn phases and similar but somewhat different chemistry for the Al_6Mn and $MgZn_2$ phases. The chemical composition of the metastable $MgZn_2$ phase (see figure 39) has long been of interest, and JMatPro provides a metastable-based calculation of elemental composition for 7075 that may be compared to the equilibrium $MgZn_2$ phase (see figures 37 and 38). From inspection of the JMatPro plots, it may be seen that the 7020 and 7075 phase precipitates have similar chemistry and may be assumed to have corresponding similar physical properties.

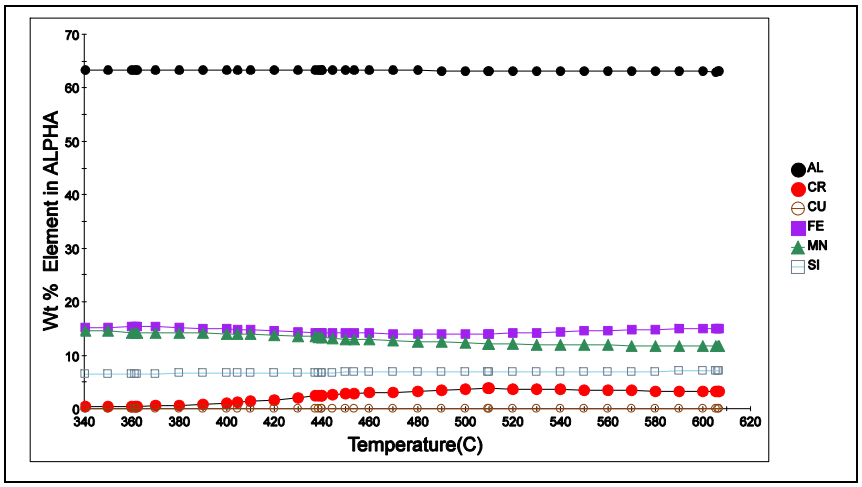

Figure 31. JMatPro calculated weight-percent of elements in 7020 α AlFeMnSi phase.

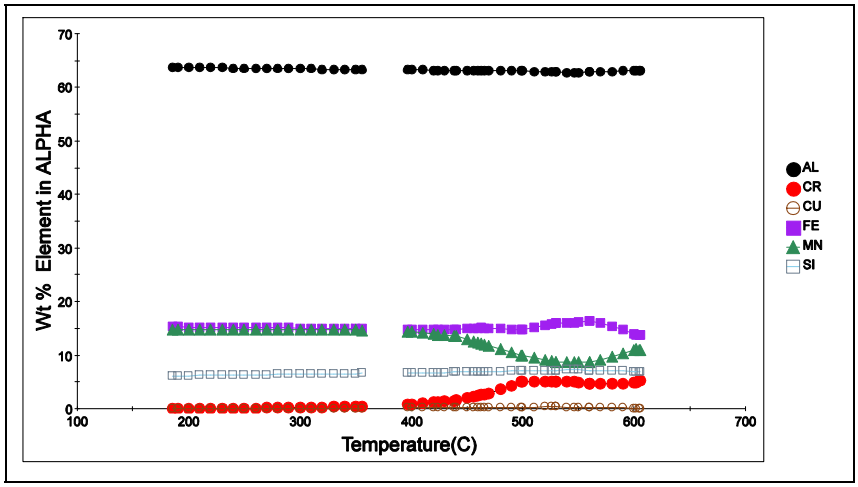

Figure 32. JMatPro calculated weight-percent of elements in 7075 α AlFeMnSi phase.

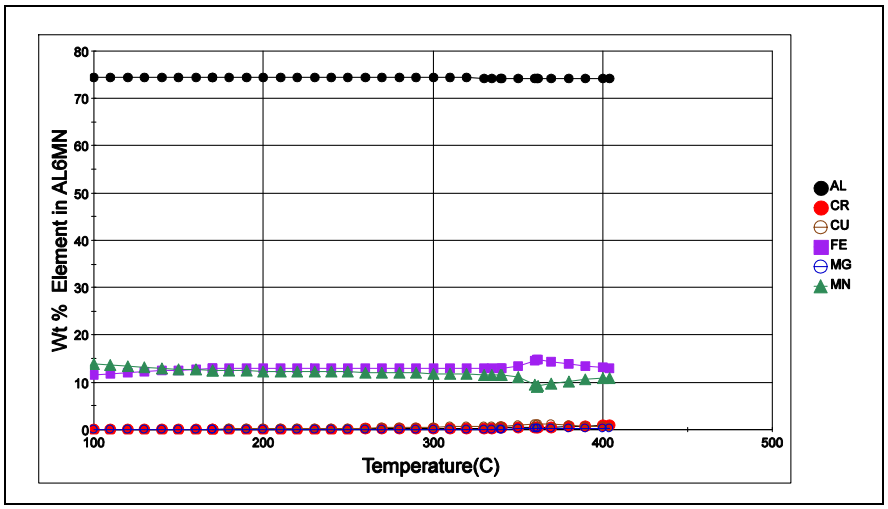

Figure 33. JMatPro calculated weight-percent of elements in 7020 Al_6Mn phase.

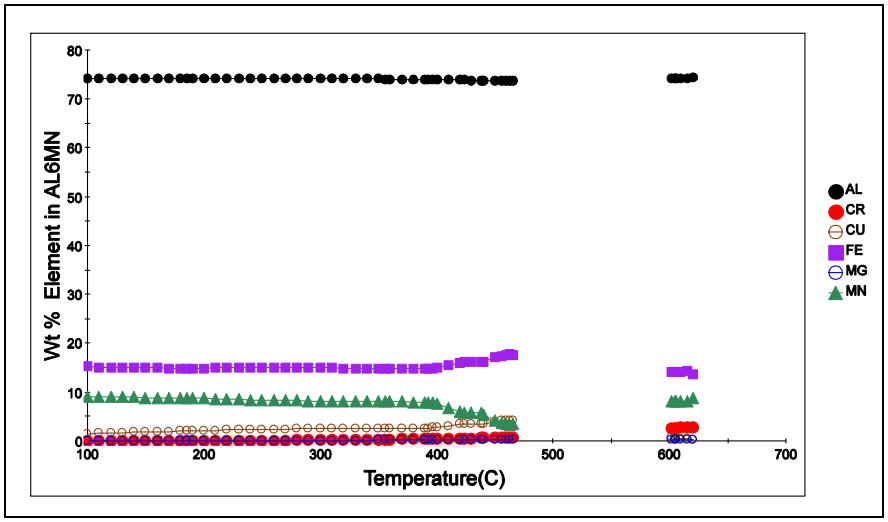

Figure 34. JMatPro calculated weight-percent of elements in 7075 Al_6Mn phase.

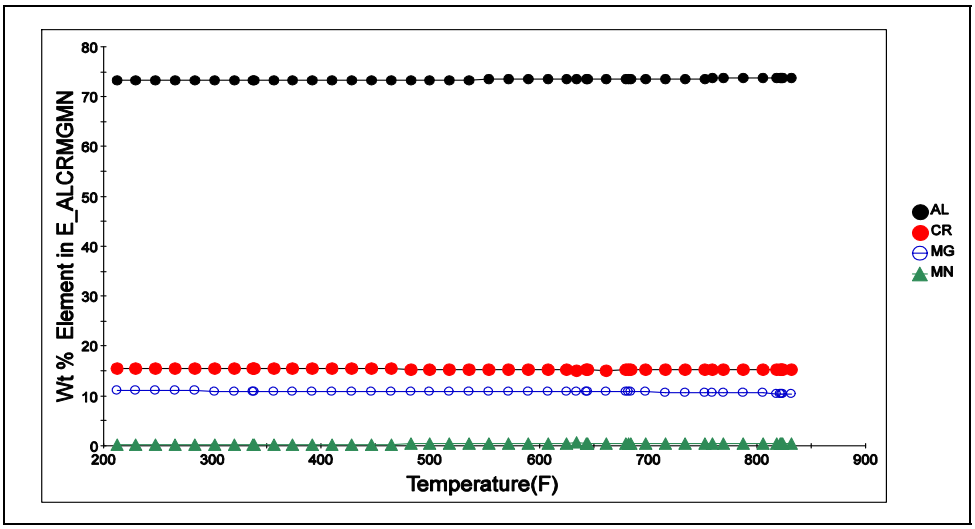

Figure 35. JMatPro calculated weight-percent of elements in 7020 E AlCrMgMn phase.

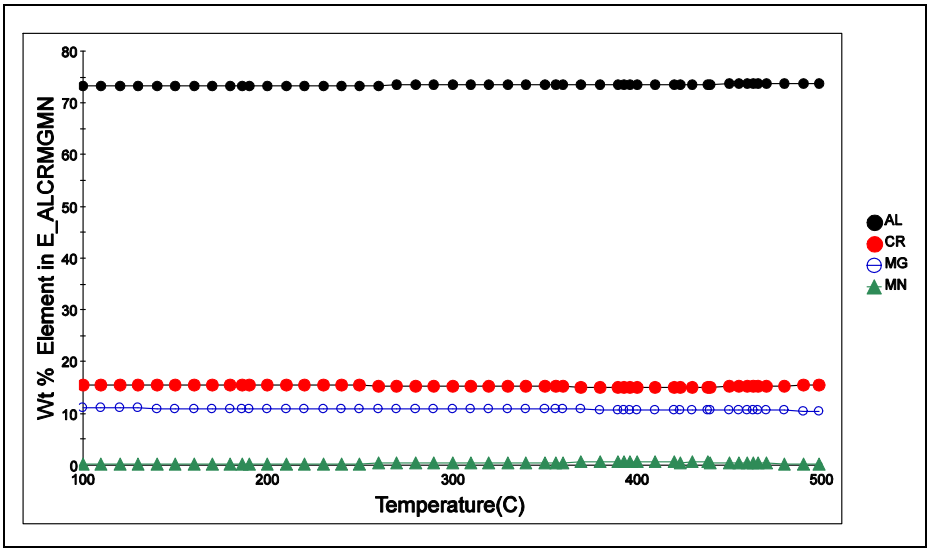

Figure 36. JMatPro calculated weight-percent of elements in 7075 E AlCrMgMn phase.

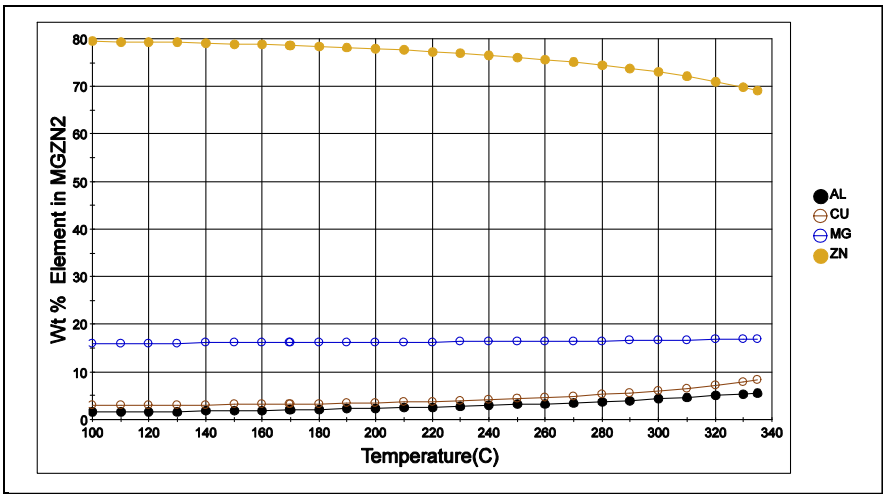

Figure 37. JMatPro calculated weight-percent of elements in 7020 $MgZn_2$ phase.

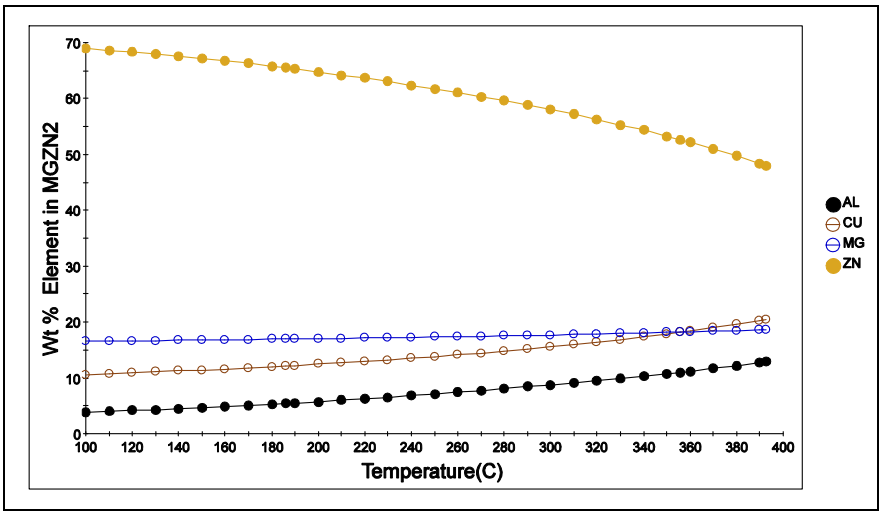

Figure 38. JMatPro calculated weight-percent of elements in 7075 $MgZn_2$ η phase.

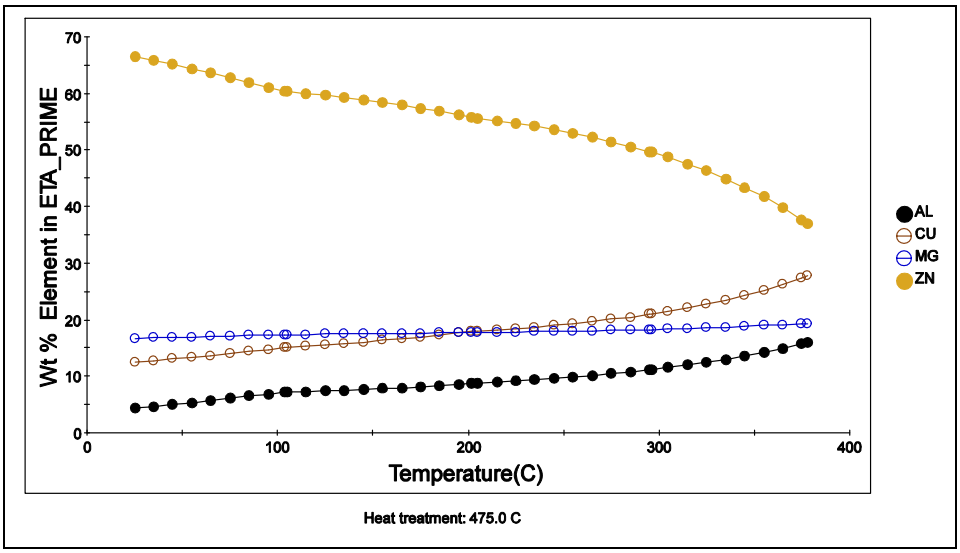

Figure 39. JMatPro calculated weight-percent of elements in 7075 $MgZn_2$ ή phase.

3.3.8 JMatPro Thermophysical Properties Derived From Gibbs Free Energy

Thermophysical (*7*–*9*) properties of materials may be derived from Gibbs free energy (see formulas A1–A9 in the appendix), as with the temperature-dependent properties of elastic moduli (see formulas A8 and A9 in the appendix) of phases predicted by JMatPro. Examples of JMatPro capabilities for TS calculations of physical properties include plots of shear and bulk moduli for 7075 aluminum and constituent phases (see figures 40 and 41). The plot of shear modulus (see figure 40) at 25 °C for 7075 aluminum reveals that without great variance, the 7075 shear modulus values are largely within one of the following two distinct groups: (1) high elastic strength or (2) elastic strength approximate to the matrix. The JMatPro calculations of the 7075 bulk moduli (see figure 41) share a group but have greater variance. The constituent phases that are common to 7075 and 7020 include α AlFeMnSi, Al_6Mn, E AlCrMgMn, and $MgZn_2$ (see figures 31–38), and these solution-treated and aged materials are likely to have both the $MgZn_2$ phase from aging and the α AlFeMnSi phase inherited from solution treatment. With exception to $MgZn_2$, these phases are present in 7039 (see figure 23).

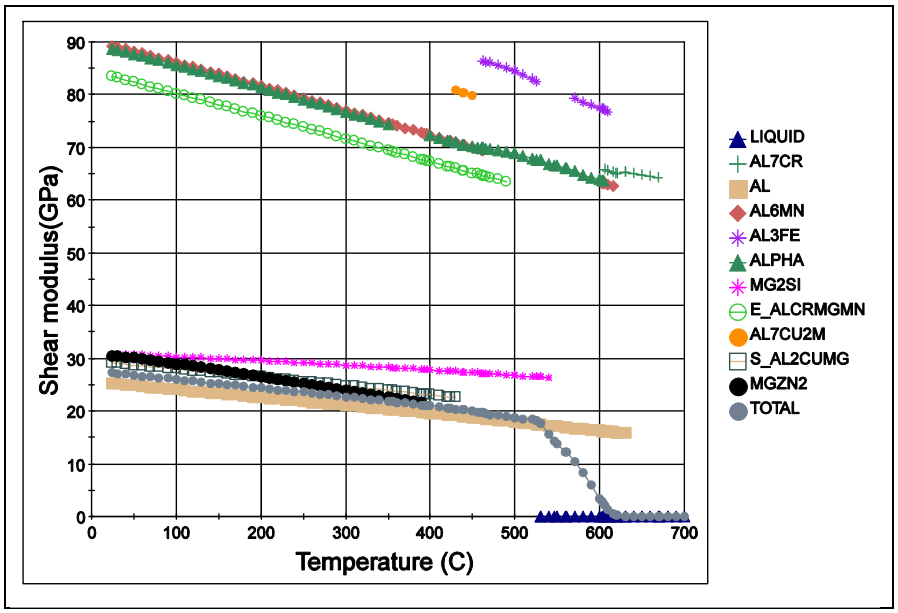

Figure 40. JMatPro calculated TS plot of shear moduli, G, for 7075 aluminum alloy.

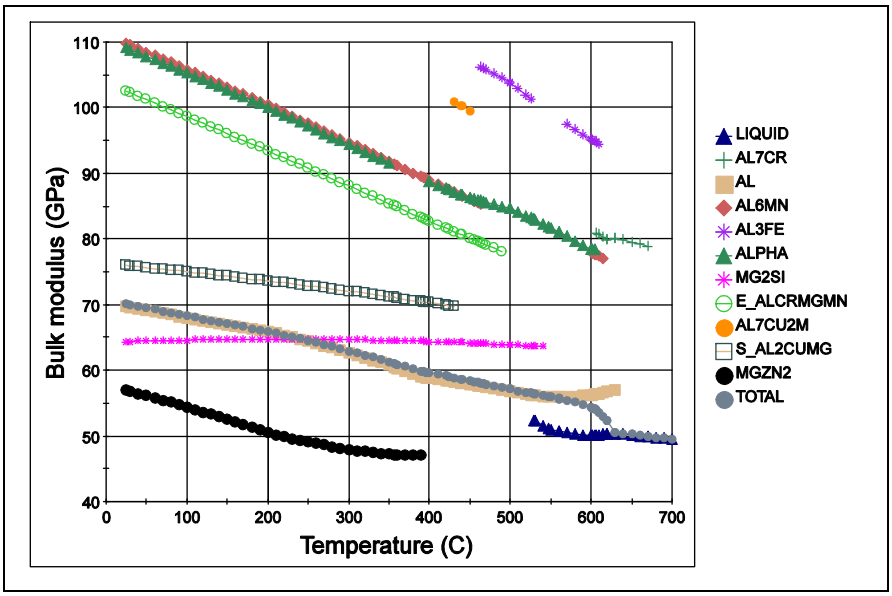

Figure 41. JMatPro calculated TS plot of bulk moduli, K, for 7075 aluminum alloy.

The 7020, 7039, and 7075 materials in this study are inhomogeneous, containing many separate distinct particle constituents and phases of greatly different elastic moduli, so that misfit stresses may arise on the microscale, even under conditions of hydrostatic pressure (*27–29*). In homogeneous materials, hydrostatic pressure provides no deviatoric stress and therefore no plastic deformation, as determined by the Von Mises criterion (*30*). Hydrostatic pressure is

significant to materials processing and applications, as it is desired to assist formability of metals by sustaining deformation without fracture, and it is a significant component of the stress state encountered in pressure vessels at significant depths in the ocean or earth, in vicinity of shock waves propagating through solids, or in the result of thermal expansion coefficient differences between a composite matrix and reinforcement material. High hydrostatic pressure suppresses void growth, thereby delaying fracture. Hydrostatic tension accelerates void growth (*29–32*). It is reasonable to apply JMatPro calculated values of elastic moduli to models that predict microscale shear stress to evaluate the sensitivity and capability of microconstituent particles to induce plasticity (*27–29*) or microcracking on the surrounding matrix material under loading by hydrostatic pressure or stress (*30*).

3.3.9 Application of JMatPro Thermophysical Elastic Moduli: Models for Dislocation Generation Under Hydrostatic Pressure and for Incipient Spall Failure

The stresses required to homogeneously nucleate dislocations in pure, defect-free metals are high, and it is far easier to nucleate dislocations heterogeneously on interfaces with grain boundaries, surfaces, precipitates, dispersed phases, or reinforcing fibers. One mechanism in which inclusions, impurities, and microconstituent particles may affect dislocation generation is through local levels of shear stresses that may be developed around inclusions and other defects developed from differences in compressibility between the matrix and second phase particles. Dislocations are generated in materials when shear stress, τ_{max}, reaches the nucleation shear stress for dislocation generation, which may be low as 0.7–10 MPa, as observed in metal crystals. Maximum shear stress at a matrix/second phase interface has been estimated by Das and Radcliffe (*27*) and by Ashby et al. (*28*) for conditions of hydrostatic stress acting on spherical elastic inclusions surrounded by an isotropic matrix as follows:

$$\tau_{\max} = \frac{3G_m}{K_m}\left(\frac{K_m - K_p}{3K_p + 4G_m}\right)P , \tag{32}$$

where G_m = the shear modulus of the matrix, K_m and K_p = the bulk moduli of the matrix and second phase, respectively, and P = the applied hydrostatic pressure.

The Das-Radcliffe or Ashby, Gelles, and Tanner (DR-AGT) model calculates values of maximum shear stress with respect to the shear modulus of the matrix and the bulk moduli of the matrix and particle without regard to lattice parameters or orientations for dislocation slip, surface irregularity, or particle size. With application of the maximum shear stress model, the experimental pressurization tests and microstructural examinations conducted by Ashby et al. (*28*) revealed that dislocation generation around particles subjected to hydrostatic stress is dependent on a critical size of inclusion particle that is best described by the relation

$$p_{crit} = Ar_o^n , \tag{33}$$

constant, and n = 0.6 ± 0.3 such that large particles 1400–2000 Å (140–200 nm or 0.14–0.2 μm) more easily cause significant dislocation generation at low pressures as low as 5–10 kbar

(0.5–1.0 GPa), and smaller particles require significantly greater pressure around and over 30 kbar (3 GPa). It was also observed that a particle's shape had a significant effect on dislocation generation such that non-spherical particles were more effective in dislocation generation than spheres, and dislocations were strongly generated or not at all.

Results of calculations with the DR-AGT maximum shear stress model using JMatPro calculated bulk moduli for 7075 alloy and its constituents at 25 °C are shown (see table 12) for hydrostatic pressures of 1.05–3.3 GPa. The 1.05–3.3 GPa range of pressures are those experimentally observed and theoretically calculated by Chevrier and Klepaczko (*31*, *32*) to be necessary for time and load-dependent incipient spall failure in 7020. It is generally understood that the first stage of spall is controlled by a critical stress level linked to the microstructure and that the spall damage is a result of tensile stress created by reflection of compressive waves at interfaces. The Chevrier and Klepaczko thermodynamic, time, and load-dependent models reveal that short times of impact loading require higher values of stress in tension, and longer times require lower levels of stress that overall determine a critical time and stress level.

Table 12. Microscale maximum shear stress (*27*, *28*) calculated from JMatPro 7075 bulk and shear moduli and imposed macroscopic hydrostatic stress.

7075 Alloy Material			**Hydrostatic Pressure Load Condition p (GPa)**					
			3.3	**1.95**	**1.80**	**1.37**	**1.2**	**1.05**
Bulk Moduli, 25 °C			**Calc. Max. Induced Shear Stress (τ)**					
Phase	**G (GPa)**	**A[a]**	**GPa**					
Al_6Mn	109.76	–0.105	–0.348	–0.205	–0.190	–0.144	–0.126	–0.111
α AlFeMnSi	109.11	–0.104	–0.344	–0.203	–0.187	–0.143	–0.125	–0.109
E_AlCrMgMn	102.51	–0.091	–0.299	–0.177	–0.163	–0.124	–0.109	–0.095
S_Al_2CuMg	75.93	–0.020	–0.066	–0.039	–0.036	–0.028	–0.024	–0.021
Total 7075	70.11	0.000	0.000	0.000	0.000	0.000	0.000	0.000
Al	69.71	0.001	0.005	0.003	0.003	0.002	0.002	0.002
Mg_2Si	64.34	0.022	0.073	0.043	0.040	0.030	0.027	0.023
$MgZn_2$	56.90	0.055	0.182	0.107	0.099	0.075	0.066	0.058

[a] $\tau_{max} = \frac{3G_m}{K_m}\left(\frac{K_m - K_p}{3K_p + 4G_m}\right)P = Ap.$

Notes: The JMatPro calculated shear modulus for 7075 at 25° C = 27.2 GPa. The Von Mises effective stress for shear stress in pure shear = k = $Y/\sqrt{3}$ = $350/\sqrt{3}$ = 202 MPa 7020-T651, $443/\sqrt{3}$ = 256 MPa 7075-T7351, and $552/\sqrt{3}$ = 319 MPa 7075-T651, where Y = uniaxial yield stress.

The Al_6Mn, E AlCrMgMn, α, Mg_2Si, and Al_3Fe phases for 7020 and 7075 (see figures 31–36) reveal similar elemental compositions, and it may be assumed that these phases will likely share similar values of elastic moduli in 7020 and 7075. The $MgZn_2$ phase for T7 tempers, however, may have some variation in properties with Cu content. The respective values of shear and bulk moduli for 7075 and 7020 are known to be near equal. It may be seen that the JMatPro calculated levels of bulk moduli for Al_6(FeMn), α (AlFeMnSi), and E (AlCrMgMn) phases

considerably exceed those of the 7075 or 7020 matrices and that the S Al_2CuMg and $MgSi_2$ phases have bulk moduli strengths approximate to the total (matrix) materials. The $MgZn_2$ phase has moderately less bulk modulus strength than the matrix.

Whether load is applied in tension or compression, the mechanism of deformation of metals in the macroscale and microscale is through shear deformation. The Von Mises criterion (*30*) postulates that yielding will occur when some value of the root-mean shear stress reaches a constant,

$$[(\sigma_1 - \sigma_2)^2 + (\sigma_2 - \sigma_3)^2 + (\sigma_3 - \sigma_1)^2/3]^{1/2} = C_1. \quad (34)$$

Equivalently,

$$(\sigma_1 - \sigma_2)^2 + (\sigma_2 - \sigma_3)^2 + (\sigma_3 - \sigma_1)^2 = C_2, \quad (35)$$

where for any general stress state, σ_1, σ_2, and σ_3 are the principal stresses of a set of axis where applied shear stresses are zero. Stress states of uniaxial tension and simple shear may be used to define the constant C_2 and establish a proportional relation of yielding between the states of uniaxial tension and simple shear.

With uniaxial tension at yielding,

$$\sigma_1 = Y, \sigma_2 = \sigma_3 = 0, C_2 = 2Y^2, \quad (36)$$

and with pure shear at yielding,

$$\sigma_1 = k = -\sigma_3, \sigma_2 = 0, C_2 = 6k^2; \quad (37)$$

therefore,

$$k = Y/\sqrt{3}. \quad (38)$$

By use of equation 38, the range of maximum shear stress (see table 9) values generated by particle-matrix misfit under hydrostatic loads in compression by high-elastic-strength particles can be seen to contain shear stress values also determined by the value of the root mean shear stress of the Von Mises criterion equal to 202 MPa for 7020 alloy certificate values of 350 MPa uniaxial tension yield strength, Y, (*23*, *25*) and the shear strength values, k, of 256 and 319 MPa, determined by experimentally determined values of tensile yield strength for 7075-T7351 and 7075-T651, respectively (*26*). The equivalent values of particle misfit shear stress and shear yield stress occur at a hydrostatic pressure load of 1.95 GPa for 7020 that corresponds to a load time for spall near 1-μs duration (*31*, *32*). It may also be observed that particles of the Al_6Mn, α AlFeMnSi, and E AlCrMgMn phases, common to 7020, 7039, and 7075 (see figures 31–36), induce the greatest levels of shear stress. Figure 42 plots the microscopic maximum shear stress data from table 12 as the response of imposed macroscopic pressure over the range of the

1.05–3.3 GPa hydrostatic pressures necessary for incipient spall in 7020 that respectively correspond to ~7020 spall load time intervals of 2–0.5 μs. The predicted levels of microscopic shear stress reveal that dislocation generation or microdamage may easily occur even during the compression stage portion of loading of high-strength materials during the process of spallation. In a similar manner, these constituent particles may preferentially nucleate dislocations during metal working under compression stress or serve as nucleation sites for void nucleation and growth or microcracking under tension or shear loading. These predictions suggest in some cases that fracture ductility during spall may be enhanced by microconstituent particles, as opposed by material failure that may occur solely by localized crack propagation. Comparable relationships of pressure, macroscopic yield and shear stress, and microscopic shear stress near particles may be shown using JMatPro calculated values of bulk moduli for 4815 steel phases, the Von Mises criterion calculated value for shear yield stress, and the Chevrier and Klepaczko model calculated values of critical spall stress of steel. In addition, based on the strength levels of these Al materials, 7020 is expected to have greater resistance to spall based also on critical sizes of flaw through levels of applied stress required for failure through crack propagation (*34*).

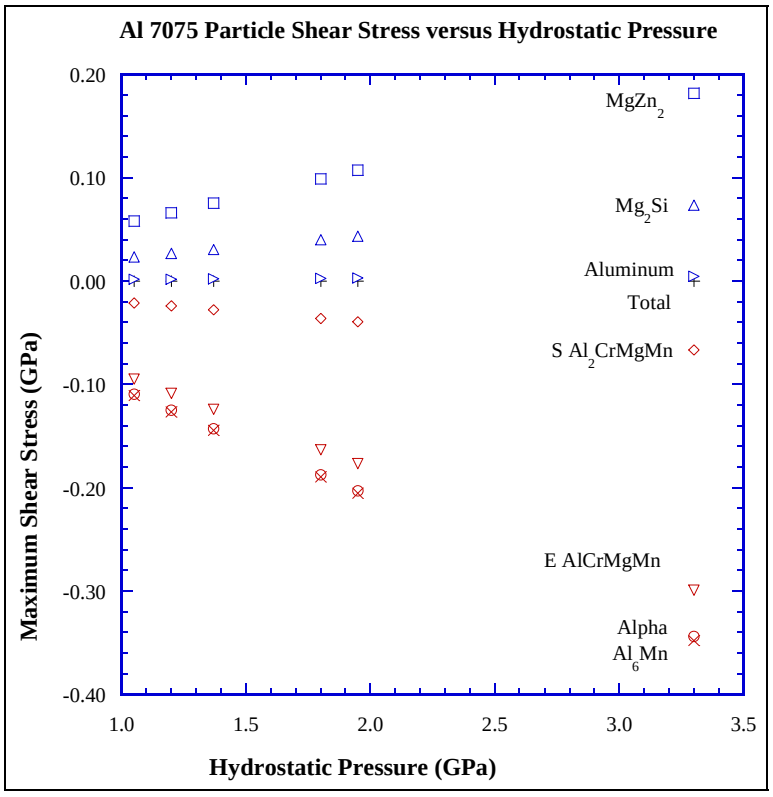

Figure 42. Plot of microscale maximum shear stress calculated by DR-AGT model and JMatPro microconstituent moduli as a result of hydrostatic pressure.

4. Conclusions

The following 10 conclusions were reached in this report:

1. TTT and CCT curves reveal that the critical times for onset of phase transformation for alloy 7020 are greater than those of 7039 and 7075 such that low rates of cooling may be used, which is beneficial for maintaining mechanical properties of strength and ductility and eliminating residual stress of quenched plate and a potential causal factor of SCC.
2. TS plots of partial Gibbs energy of elemental components of the weight-percent equilibrium phases, elemental composition of liquid, and elemental compositions of phases provide useful information for selection of process parameters, predicting times and temperatures for solution treatment, quenching of structures, age hardening, and predicting mechanical properties of deformation and fracture.
3. The TTT and CCT and the TS plots and calculations appear useful for prediction of applicability of the alloys as to potential application, such as structural protection materials for vehicles, where concerns include (1) the ability to manufacture thick plate without residual stress or loss of mechanical properties, (2) the ability to fabricate plate by fusion weld processes, and (3) Cu microalloy of $MgZn_2$ phase effectiveness for measures to improve resistance to SCC.
4. For the 2XXX Cu, 3XXX Mn, 4XXX Si, 5XXX Mg, 6XXX Si + Mg, and 7XXX Mg-Zn-Mg-(Cu) Al alloys, the partial Gibbs energy TS plots reveal the Zn and Mg elements have partial Gibbs energies nearest that of aluminum. The Cu, Si, or Mn elements have significantly greater partial Gibbs energy that may be of concern in processing or service.
5. Weight-percent equilibrium TS plots reveal alloy advantages of 7020 in amount of hardening and constituent phases that are able to undergo dissolution to minimize residual particle content and a high solidus temperature that minimizes risks of harmful liquation effects during solution treatment.
6. TS plots of elemental compositions of liquid reveal partitioning of elements during eutectic solidification that is greatest to least with Si, Cu, Mg, and Zn as measured by ratio of the weight-percent of elements in the solid at the solidus temperature over the weight-percent of elements in the alloy at the liquidus temperature S/L.
7. Weight-percent of elements in phase with Cu reveal the capability of the $MgZn_2$ phase that may better resist hydrogen embrittlement mechanism of the 7XXX alloys. The elemental composition of the Al_6Mn, Alpha AlFeMnSi, and E AlCrMgMn phases for both 7075 and 7020 appear sufficiently similar to allow the assumption that their physical properties are similar.

8. Derivative values of Gibbs energy, such as thermophysical properties of density, specific heat, and elastic moduli of the alloy and constituent phases, may be useful for prediction of industrial processes like casting and welding and deformation and fracture behavior.
9. The physical properties of elastic bulk moduli for constituent particles, derived from Gibbs energy by JMatPro, may be used together with theoretical models of DR-AGT to predict the maximum levels of microscale shear stresses around constituent particles under hydrostatic pressure. Within the pressure-time conditions shown by Chevrier and Klepaczko (*31*, *32*) to cause thermodynamic dependent incipient spall in 7020 alloy, the high-elastic-strength particles induce the greatest maximum shear stress, and these microscale shear stress levels may equal or exceed the level of Von Mises calculated shear stress of 7020 alloy, revealing that dislocation generation and micro shear deformation may occur during the initial stages of compression during spall events. These constituent particles may preferentially nucleate dislocations during metal working under compression stress or serve as nucleation sites for void nucleation and growth or microcracking under macroscopic tension or shear loading.
10. Use of the computational thermodynamic program JMatPro provides better understanding of thermodynamic concepts and reveals that the high-Zn, low-Mg alloy components of 7020 provide more optimal thermodynamic phase stability and transformations for low cost alloy manufacture, processing, fabrication, and service as a protection material.

5. References

1. National Research Council. *Integrated Computational Materials Engineering*; National Academy of Sciences: Washington, DC, 2008.
2. Saunders, N.; Kucherenko, S.; Li, X.; Miodownik, A. P.; Schille, J. P. A New Computer Program for Predicting Materials Properties. *J. of Phase Equilibria* **2001**, 22 (4).
3. Saunders, N. The Modeling of Stable and Metastable Phase Formation in Multi-Component Al-Alloys. *Proceedings of the 9th International Conference on Aluminum Alloys*, Brisbane, Australia, 2–5 August 2004.
4. Saunders, N. The Application of Calculated Phase Equilibria to Multi-Component Aluminum Alloy. *J. JILM* **2001**, 51.
5. Guo, Z.; Saunders, N.; Schille, J. P.; Miodownik, A. P. Material Properties for Process Simulation. *Mat. Sci. and Eng.: A* **2009**, *499*, 7–13.
6. Thermotech Databases. http://www.thermotech.co.uk/databases.html (accessed July 2011).
7. Porter, D. A.; Easterling, K. E. *Phase Transformations in Metals and Alloys*, Van Nostrand Reinhold: New York, NY, 1981.
8. Lukas, H. L.; Fries, S. G.; Sundman, B. *Computational Thermodynamics, the Calphad Method*; Cambridge University Press: Cambridge, UK, 2007.
9. Gaskell, D. R. *Introduction to Metallurgical Thermodynamics*; 2nd ed.; Hemisphere Publishing Corp. and McGraw-Hill Book Company: New York, NY, 1981.
10. Thermodynamic Databases for Thermo-Calc. http://www.thermocalc.com/TCDATA.htm (accessed July 2011).
11. CALPHAD. http://www.calphad.org (accessed July 2011).
12. Hatch, J. E., Ed. *Aluminum Properties and Physical Metallurgy*; American Society for Metals: Metals Park, OH, 1984.
13. Mondolfo, L. F. The Structure of the Aluminum: Magnesium: Zinc Alloys. *Metallurgical Reviews* **1971**, *16* (153), 95–124.
14. Nils, R. Precipitation Kinetics in an Al-Zn-Mg-Alloy. *Zeitschrift für Metallkund* **1975**, *66* (6), 338–343.
15. Inoue, H.; Sato, T.; Kojima, Y.; Takahashi, T. The Temperature Limit for GP Zone Formation in an Al-Zn-Mg Alloy. *Met. Trans. A* **1981**, 12A.

16. Deschamps, A.; Texier, G.; Ringeval, S.; Delfaut-Durut, L. Influence of Cooling Rate on the Precipitation Microstructure in a Medium Strength Al-Zn-Mg Alloy. *Mat. Sci. and Eng.* **2009**, *A501*, 133–139.

17. Deschamps, A.; Bréchet, Y. Influence of Quench and Heating Rates on the Ageing Response of an Al-Zn-Mg-(Zr) Alloy. *Mat. Sci. and Eng.* **1998**, *A251*, 200–207.

18. Waterloo, G.; Hansen, V.; Gjønnes, J.; Skjervold, S. R. Effect of Predeformation and Presaging at Room Temperature in Al-Zn-Mg-(Cu,Zr) Alloys. *Mat. Sci. and Eng.* **2001**, *A303*, 226–233.

19. Polmear, I. J. *Light Alloys*; 4th ed.; Elsevier: London, UK, 2006.

20. Gruhl, W. Stress Corrosion Cracking of High Strength Aluminum Alloys. *Z. Metallkde Bd.* **1984,** *75 H.11*, 819–826.

21. Holroyd, N. J. H.; Hardie, D. Effect of Inherent Defects on Initiation of Stress-Corrosion Cracks in Weldable Al-Zn-Mg Alloys. *Mets. Tech.* **1982**, *9*, 229–234.

22. Int. Alloy Designations and Chem. Comp. Limits for Wrought Al. and Wrought Al. Alloys. http://www.eaa.net/upl/4/default/doc/tealsheets 2009.pdf (accessed February 2009).

23. EN 10204/3.1 Inspection Certificate Technological Properties: (a) Aleris Al. Koblenz Gmbh 12-mm plate, 29 January 2008; 25-mm plate, 11 January 2007; and 50-mm plate, 14 June 2007; and (b) Alcan Al. Valais (Sierre) 40-mm plate, 9 January 2008.

24. Chase, M.; Kackley, N.; Bethoney, W. Engineering and Ballistic Properties of a Newly Developed 2XXX Series Aluminum Alloy Armor Published by the Royal Military College of Science. *Proceedings of the 9th International Symposium on Ballistics*, Shrivenham, UK, 29 April–1 May 1986; session VI, pt. 2, pp 511–521.

25. Chinella, J. F. Development of Low Cost, High Performance AlZn4.5Mg1 Alloy 7020. In *Aluminum Alloys: Fabrication, Characterization and Applications II*; Yin, W. et al., Eds. The Minerals, Metals, and Materials Society: San Francisco, CA, 16 February 2009.

26. Chinella, J. F.; Jones, T. *Evaluation of Commercial Aluminum Alloys for Armor and Vehicle Upgrade*; ARL-TR-4596; U.S. Army Research Laboratory: Aberdeen Proving Ground, MD, September 2008.

27. Das, G.; Radcliffe, S. V. Pressure-Induced Development of Dislocations at Elastic Discontinuities. *Philos. Mag.* **1969**, *20*, 589.

28. Ashby, M. F.; Gelles, S. H.; Tanner, L. E. The Stress at Which Dislocations Are Generated at a Particle-Matrix Interface. *Philos. Mag*. **1969**, *19*, 757.

29. Lewandowski, J. J.; Lowhaphandu, P. Effects of Hydrostatic Pressure on Mechanical Behavior and Deformation Processing of Materials. *Int. Matls. Revs*. **1998**, *43* (4).

30. Hosford, W. F.; Caddell, R. M. *Metal Forming Mechanics and Metallurgy*; Prentice-Hall, Inc.: Englewood Cliffs, NJ, 1983; pp 32–37.

31. Chevrier, P. F.; Klepaczko, J. R. Spalling of Aluminum Alloy 7020-T6, Experimental and Theoretical Analysis, in Mechanisms and Mechanics of Damage and Failure. *Proceedings of the 11th Biennial European Conference on Fracture*, Poitiers-Futurosc, France, 1996; pp 693–698.

32. Chevrier, P. F.; Klepaczko, J. R. Spall Fracture: Mechanical and Microstructural Aspects. *Eng. Fracture Mech.* **1999**, *63*, 273–294.

33. Grzemba, B.; Cordier, H.; Gruhl, W. Intercrystalline Cracking of Welded Joints in AlZnMg Alloys. *Aluminum* **1987**, *63* (5), 496–503.

34. Hertzberg, R. W. *Deformation and Fracture Mechanics of Engineering Materials*, 3rd ed.; John Wiley and Sons, Inc.: Hoboken, NJ, 1989.

Appendix. Thermotech Ltd. and Sente Software Ltd., Thermo-Physical Quantities, JMatPro Temperature Step Calculations, and 7020 and 7075 Experimental Chemistry and Microstructures

This appendix appears in its original form, without editorial change.

Section 1A: Thermotech Ltd. and Sente Software Ltd.

JMatPro is a product of:

Sente Software Ltd.
Surrey Technology Centre
40 Occam Road
GU2 7YG
United Kingdom

JMatPro uses the Thermotech* databases as an integral part of its software to run calculations. Thermotech produces a number of databases for use with thermodynamic calculation software packages. They are an integral part of JMatPro. The databases can also be used with third party software such as Thermo-Calc.

The following (alloy) databases (DATA) are available: Al; Co; Fe; Mg; Ni; Ti; Solder; Zr.

The Al database for Al-alloys contains the following elements,
Al, B, C, Ca, Co, Cr, Cu, Fe, H, La, Li, Mg, Mn, Ni, Pb, Sc, Si, Sn, Sr, Ti, V, Zn, Zr

with data for the following phases:

AL, LIQUID, AL11RE3_ALPHA, AL13CR4SI4, AL20CU2MN3, AL2CU,
AL2SI2M, AL3FE, AL3M_DO22, AL3M_DO23, AL3M_L12, AL3NI,
AL3NI2, AL3RE_DO19, AL4C3, AL4M_D13, AL4SIC4, AL5CU2MG8SI6,
AL6MN, AL7CR, AL7CU2M, AL7CU4NI, AL8FEMG3SI6, AL8SIC7,
AL9M2, ALFESI_ALPHA, ALFESI_BETA, ALLI, AL3MG2, ALLISI, ALPHA,
E_ALCRMGMN, GRAPHITE, ZN_HCP, MGZN2, MB2, MC, MG2SI,
MG2X_C1, PB_FCC, LIQ_2, R_ALCULI, SIC, SILICON, S_AL2CUMG,
T1_ALCULI, T1_PRIME, T2_ALCULI, TAU_ALLIMG, TB_ALCULI,
T_ALCUMGZN, SN, AL13CO4, ZN_FCC, GAS.

In addition it considers the metastable phases:

GP BETA", BETA_PRIME, B_PRIME,
ETA_PRIME, S_PRIME, THETA_PRIME, T_PRIME

Thermo-Calc offers database TTAL7, the Thermotech-owned Al-based Alloys Database.

As well as providing predictions for basic phase equilibria studies for most of the major types of aluminum alloy Al-Data has been highly successful in modeling complex non-equilibrium solidification. It can also be used as a prime source of thermophysical data for input into solidification modeling packages, MTDATA, Thermo-Calc, and JMatPro (see Lukas† for an explanation of nomenclature of crystal structures).

* http://www.thermotech.co.uk/databases.html
† Lukas, H. L; Fries, S. G; and Sundman, B. *Computational Thermodynamics, the Calphad Method*; Cambridge University Press: Cambridge, UK, 2007.

Section 2A: Thermo-Physical Quantities

Gibbs energy (A1) $\mathrm{G} = \mathrm{G}(T, p, N)$

Entropy (A2) $S = -\left(\frac{\partial G_m}{\partial T}\right)_{p,N_i}$

Enthalpy (A3) $\mathrm{H} = \mathrm{G} + \mathrm{TS} = \mathrm{G} - \mathrm{T}\left(\frac{\partial G}{\partial T}\right)_{p,N_i}$

Volume (A4) $\mathrm{V} = \left(\frac{\partial G}{\partial p}\right)_{T,N_i}$

Chemical potential of component, i, (A5) $\mu_i = \left(\frac{\partial G}{\partial N_i}\right)_{T,p,N_{j\neq i}}$

Heat capacity (A6) $C_p = -\mathrm{T}\left(\frac{\partial^2 G}{\partial T^2}\right)_{p,N_i} = \frac{\Delta Q}{\Delta t}$

Thermal expansion (A7) $\propto = \frac{1}{V}\left(\frac{\partial^2 G}{\partial p \partial T}\right)_{N_i} = \frac{1}{V}\left(\frac{\delta V}{\delta T}\right)_p$

Isothermal Compressibility (A8) $\kappa = -\frac{1}{V}\left(\frac{\delta^2 G}{\delta \rho^2}\right)_{T,n_i} = -\frac{1}{V}\left(\frac{\delta V}{\delta p}\right)_T$

Bulk Modulus (A9) $\beta = {}^{1}/_{\kappa} = -V\frac{\delta P}{\delta V}$

Section 3A: JMatPro Temperature Step Calculations of Equilibrium Phases

Table A1. JMatPro temperature step calculations of phases for Al 7020.

Temp. (º C)	7020 Phase (w%)										
	Liquid	Al_3M DO23	Al_7Cr	Al	Al_3Fe	Alpha	Al_9M_2	E AlCrMgMn	Al_6Mn	Mg_2Si	$MgZn_2$
700.000	99.95	0.05									
690.000	99.92	0.08									
680.000	99.89	0.11									
670.000	99.87	0.13									
660.000	99.84	0.16									
650.000	99.82	0.18									
648.897	99.82	0.18	0.00								
646.495	99.77	0.18	0.05	0.00							
645.899	96.04	0.16	0.00	3.80							
640.000	62.60	0.05		37.35							
632.186	35.56	0.00		64.44							
630.000	30.54			69.46							
628.642	27.81			72.19	0.00						
620.000	11.65			87.90	0.44						
610.000	2.56			96.79	0.65						
606.729	0.81			98.50	0.69	0.00					
606.445	0.63	0.00		98.67	0.68	0.02					
605.393	0.00	0.00		99.24	0.66	0.10					
600.000		0.01		99.17	0.62	0.19					
590.000		0.04		99.05	0.57	0.35					
580.000		0.06		98.94	0.52	0.49					
570.000		0.08		98.83	0.47	0.62					
560.000		0.09		98.74	0.43	0.73					
550.000		0.11		98.65	0.40	0.83					
540.000		0.13		98.58	0.37	0.93					
530.000		0.14		98.50	0.35	1.01					
520.000		0.15		98.44	0.33	1.08					
510.000		0.17		98.37	0.32	1.14					
509.703		0.17	0.00	98.37	0.32	1.14					
500.000		0.18	0.08	98.27	0.29	1.19					
490.000		0.19	0.15	98.17	0.26	1.23					
480.000		0.20	0.22	98.08	0.24	1.27					
470.000		0.21	0.28	97.99	0.22	1.30					
460.000		0.21	0.35	97.91	0.20	1.33					
453.599		0.22	0.38	97.86	0.19	1.35	0.00				
450.000		0.22	0.40	97.84	0.18	1.36	0.00				
444.473		0.23	0.44	97.80	0.16	1.37	0.01	0.00			
440.000		0.23	0.10	97.70	0.20	1.39	0.00	0.37			
439.627		0.23	0.08	97.69	0.21	1.40	0.00	0.40			
438.521		0.23	0.00	97.67	0.22	1.40		0.48			
437.051		0.23		97.65	0.21	1.40	0.00	0.50			
430.000		0.24		97.56	0.19	1.42	0.00	0.59			
420.000		0.24		97.45	0.17	1.44	0.01	0.69			
410.000		0.25		97.36	0.14	1.46	0.02	0.78			
404.311		0.25		97.31	0.13	1.47	0.02	0.82	0.00		
400.000		0.25		97.27	0.12	1.47	0.02	0.85	0.01		
390.000		0.26		97.19	0.09	1.49	0.02	0.91	0.04		
380.000		0.26		97.13	0.06	1.50	0.03	0.96	0.06		
370.000		0.27		97.07	0.04	1.51	0.03	1.00	0.09		
362.227		0.27		97.02	0.02	1.51	0.03	1.02	0.12	0.00	
361.474		0.27		96.99	0.00	1.46	0.04	1.03	0.21	0.01	
360.000		0.27		96.96		1.38	0.04	1.03	0.30	0.02	
350.000		0.28		96.68		0.71	0.04	1.04	1.11	0.14	
340.227		0.28		96.38		0.00	0.04	1.04	1.99	0.27	
340.000		0.28		96.38			0.04	1.04	1.99	0.27	
334.902		0.28		96.37			0.04	1.05	1.99	0.27	0.00
330.000		0.28		96.13			0.04	1.06	1.99	0.27	0.23
320.000		0.29		95.66			0.04	1.06	1.99	0.27	0.69
310.000		0.29		95.22			0.04	1.07	1.99	0.27	1.12

300.000		0.30		94.80			0.04	1.07	1.99	0.27	1.53
290.000		0.30		94.41			0.04	1.08	1.99	0.27	1.91
280.000		0.30		94.05			0.04	1.08	1.99	0.27	2.27
270.000		0.31		93.71			0.04	1.08	1.99	0.27	2.61
260.000		0.31		93.39			0.04	1.08	1.99	0.27	2.92
250.000		0.32		93.09			0.04	1.08	1.99	0.27	3.21
240.000		0.32		92.82			0.04	1.08	1.99	0.27	3.48
230.000		0.32		92.57			0.04	1.09	1.99	0.27	3.73
220.000		0.32		92.33			0.04	1.09	1.99	0.27	3.96
210.000		0.33		92.12			0.04	1.09	1.99	0.27	4.17
200.000		0.33		91.93			0.04	1.09	1.99	0.27	4.36
190.000		0.33		91.75			0.04	1.09	1.99	0.27	4.53
180.000		0.33		91.60			0.04	1.09	1.99	0.27	4.69
170.000		0.34		91.46			0.04	1.09	1.98	0.27	4.83
169.766		0.34		91.45	0.00		0.04	1.09	1.98	0.27	4.83
160.000		0.34		91.34	0.02		0.04	1.08	1.95	0.27	4.95
150.000		0.34		91.24	0.04		0.04	1.08	1.92	0.27	5.06
140.000		0.34		91.16	0.06		0.04	1.08	1.89	0.27	5.16
130.000		0.34		91.08	0.08		0.04	1.08	1.86	0.27	5.25
120.000		0.34		91.02	0.10		0.04	1.08	1.83	0.27	5.32
110.000		0.34		90.97	0.11		0.04	1.08	1.80	0.27	5.38
100.000		0.34		90.93	0.13		0.04	1.08	1.77	0.27	5.43
Temp. (º C)	Liquid	Al_3M DO23	Al_7Cr	Al	Al_3Fe	Alpha	Al_9M_2	E AlCrMgMn	Al_6Mn	Mg_2Si	$MgZn_2$

Table A2. JMatPro temperature step calculations of phases for Al 7039.

Temp. (° C)	7039 Phase (w%)											
	Liq.	Al_3M DO2	Al_7Cr	Al	Al_3Fe	Al_9M_2	Alpha	Mg_2Si	E_AlCr -MgMn	AL_6Mn	T_ AlCuMgZn	Al_3M_ DO23
700.000	100.0											
690.000	100.0											
680.000	100.0											
670.000	100.0											
662.230	100.0	0.00										
660.000	100.0	0.00										
658.795	100.0	0.00	0.00									
650.000	99.81	0.01	0.17									
640.000	99.63	0.02	0.34									
637.750	99.60	0.03	0.38	0.00								
636.682	94.35	0.00	0.32	5.33								
630.000	68.01		0.04	31.95								
628.460	63.14		0.00	36.86								
620.000	43.09			56.91								
614.650	34.33			65.67	0.00							
610.000	27.40			72.42	0.19							
605.537	22.07			77.61	0.33	0.00						
600.000	15.72			83.59	0.22	0.47						
590.000	8.08			90.87	0.12	0.93						
588.614	7.30			91.61	0.11	0.97	0.00					
586.342	5.84			92.92	0.00	1.07	0.16					
580.000	2.99			95.57		1.10	0.34					
570.318	0.00			98.30		1.11	0.59					
570.000				98.30		1.11	0.60					
561.974				98.23		1.09	0.67	0.00				
560.000				98.22		1.10	0.68	0.01				
550.364				98.16		1.10	0.70	0.05	0.00			
550.000				98.15		1.10	0.69	0.05	0.01			
540.000				97.92		1.12	0.64	0.09	0.23			
530.000				97.72		1.13	0.60	0.13	0.42			
520.000				97.54		1.14	0.57	0.16	0.59			
510.000				97.39		1.15	0.55	0.18	0.73			
500.000				97.26		1.16	0.53	0.20	0.85			
495.656				97.21		1.16	0.52	0.21	0.90	0.00		
490.000				96.98		1.19	0.13	0.29	0.94	0.47		
488.226				96.91		1.20	0.00	0.32	0.96	0.62		
480.000				96.81		1.19		0.32	1.02	0.66		
475.365		0.00		96.76		1.19		0.33	1.05	0.68		
470.000		0.00		96.70		1.19		0.33	1.08	0.70		
460.000		0.01		96.59		1.19		0.34	1.14	0.74		
450.000		0.02		96.50		1.18		0.34	1.18	0.77		
440.000		0.03		96.42		1.18		0.35	1.23	0.80		
430.000		0.03		96.35		1.18		0.35	1.26	0.83		
420.000		0.04		96.28		1.18		0.35	1.29	0.86		
410.000		0.04		96.23		1.18		0.35	1.32	0.88		
400.000		0.05		96.18		1.18		0.35	1.35	0.89		
390.000		0.05		96.14		1.18		0.35	1.37	0.91		
380.000		0.05		96.10		1.18		0.35	1.39	0.92		
379.420		0.05		96.10		1.18		0.35	1.39	0.92	0.00	
370.000		0.06		95.54		1.18		0.35	1.40	0.93	0.53	
363.704		0.06		95.18		1.18		0.35	1.40	0.94	0.88	0.00
360.000		0.06		94.97		1.18		0.35	1.40	0.95	1.08	0.00
350.000		0.06		94.42		1.18		0.35	1.41	0.96	1.61	0.00
340.000		0.06		93.90		1.18		0.35	1.41	0.97	2.11	0.00
330.000		0.06		93.41		1.18		0.35	1.41	0.98	2.59	0.00
320.000		0.07		92.95		1.18		0.35	1.42	0.99	3.04	0.01
310.000		0.07		92.52		1.18		0.35	1.42	0.99	3.46	0.01
300.000		0.07		92.11		1.19		0.35	1.42	1.00	3.85	0.01
290.000		0.07		91.74		1.19		0.35	1.43	1.00	4.21	0.01
280.000		0.07		91.39		1.19		0.35	1.43	1.00	4.55	0.01
270.000		0.07		91.07		1.19		0.35	1.44	1.00	4.87	0.01
260.000		0.07		90.77		1.20		0.35	1.44	1.00	5.16	0.01

250.000		0.07		90.50		1.20		0.35	1.45	0.99	5.42	0.01
240.000		0.07		90.25		1.20		0.35	1.45	0.99	5.67	0.01
230.000		0.08		90.02		1.21		0.35	1.46	0.98	5.89	0.01
220.000		0.08		89.81		1.21		0.36	1.47	0.97	6.10	0.01
210.000		0.08		89.62		1.21		0.36	1.49	0.96	6.28	0.01
200.000		0.08		89.44		1.22		0.36	1.50	0.94	6.45	0.01
190.000		0.08		89.28		1.22		0.36	1.52	0.93	6.61	0.01
180.000		0.08		89.12		1.23		0.36	1.54	0.91	6.76	0.01
170.000		0.08		88.98		1.23		0.36	1.56	0.89	6.90	0.01
160.000		0.08		88.84		1.24		0.36	1.58	0.87	7.03	0.01
150.000		0.08		88.70		1.24		0.36	1.61	0.84	7.16	0.01
140.000		0.08		88.56		1.25		0.36	1.64	0.82	7.29	0.01
130.000		0.08		88.41		1.25		0.36	1.67	0.79	7.42	0.01
120.000		0.08		88.26		1.26		0.36	1.70	0.77	7.57	0.01
110.000		0.08		88.10		1.27		0.36	1.72	0.74	7.72	0.01
100.000		0.08		87.94		1.27		0.36	1.74	0.72	7.87	0.01
Temp. (° C)	Liq.	Al_3M DO2	Al_7Cr	Al	Al_3Fe	Al_9M_2	Alpha	Mg_2Si	E_AlCr -MgMn	Al_6Mn	T_ AlCuMgZn	Al_3M_ DO23

Table A3. JMatPro temperature step calculations of phases for Al 7075.

Temp. (° C)	7075 Phase (w%)										
	Liq.	Al_7Cr	Al	Al_6Mn	Al_3Fe	Alpha	Mg_2Si	E_AlCr-MgMn	Al_7Cu_2M	S_ Al_2CuMg	$MgZn_2$
700.000	100.0										
690.000	100.0										
680.000	100.0										
670.989	100.0	0.00									
670.000	99.97	0.03									
660.000	99.74	0.26									
650.000	99.52	0.48									
640.000	99.33	0.67									
630.039	99.16	0.84	0.00								
630.000	98.99	0.84	0.17								
620.000	67.12	0.66	32.22								
619.952	67.01	0.66	32.33	0.00							
615.308	55.71	0.40	43.19	0.70	0.00						
610.000	45.51	0.21	53.18	0.83	0.28						
605.676	39.01	0.10	59.53	0.92	0.44	0.00					
604.231	36.69	0.00	61.91	0.51	0.55	0.35					
602.234	33.92		64.70	0.00	0.68	0.71					
600.000	31.34		67.13		0.66	0.87					
590.000	22.32		75.64		0.53	1.51					
580.000	16.15		81.45		0.36	2.05					
570.000	11.74		85.57		0.18	2.50					
560.280	8.55		88.55		0.00	2.90					
560.000	8.47		88.62			2.90					
550.000	6.12		90.88			3.01					
546.491	5.42		91.54			3.04	0.00				
540.000	3.29		93.50			3.05	0.15				
530.000	0.86		95.77			3.07	0.30				
529.754	0.81		95.82		0.00	3.07	0.30				
525.853	0.00		96.60		0.08	2.96	0.36				
520.000			96.58		0.14	2.88	0.40				
510.000			96.56		0.24	2.75	0.45				
500.000			96.54		0.34	2.62	0.50				
498.810			96.54		0.35	2.60	0.51	0.00			
490.000			96.37		0.42	2.42	0.56	0.22			
480.000			96.21		0.48	2.26	0.61	0.44			
470.000			96.08		0.54	2.13	0.65	0.61			
465.894			96.03	0.00	0.55	2.08	0.66	0.68			
463.089			95.33	1.26	0.00	1.81	0.72	0.88			
460.000			95.26	1.34		1.73	0.73	0.93			
455.519			95.17	1.47		1.62	0.76	0.99	0.00		
450.000			95.02	1.42		1.52	0.78	1.06	0.20		

440.000			94.77	1.39		1.31	0.83	1.17	0.51		
438.144			94.73	1.41		1.27	0.84	1.19	0.57	0.00	
430.000			94.22	1.87		1.08	0.88	1.22	0.25	0.48	
423.452			93.83	2.23		0.94	0.91	1.25	0.00	0.85	
420.000			93.67	2.33		0.85	0.92	1.26		0.96	
410.000			93.21	2.69		0.55	0.98	1.31		1.25	
400.000			92.77	3.17		0.15	1.06	1.34		1.50	
396.585			92.62	3.36		0.00	1.09	1.35		1.58	
392.715			92.50	3.36			1.09	1.36		1.69	0.00
390.000			92.33	3.36			1.09	1.37		1.65	0.20
380.000			91.70	3.37			1.09	1.38		1.55	0.91
370.000			91.11	3.37			1.09	1.40		1.46	1.56
360.000			90.56	3.38			1.09	1.41		1.40	2.16
355.765			90.34	3.38		0.00	1.09	1.41		1.37	2.40
350.000			90.05	3.35		0.03	1.08	1.42		1.34	2.73
340.000			89.57	3.29		0.08	1.08	1.43		1.30	3.25
330.000			89.12	3.24		0.12	1.07	1.44		1.27	3.74
320.000			88.70	3.20		0.16	1.06	1.45		1.25	4.19
310.000			88.31	3.16		0.19	1.06	1.45		1.23	4.60
300.000			87.95	3.14		0.21	1.06	1.46		1.22	4.98
290.000			87.61	3.12		0.22	1.05	1.46		1.21	5.32
280.000			87.29	3.11		0.23	1.05	1.47		1.21	5.64
270.000			87.00	3.11		0.23	1.05	1.47		1.22	5.93
260.000			86.72	3.11		0.22	1.05	1.47		1.22	6.19
250.000			86.47	3.13		0.21	1.06	1.48		1.23	6.43
240.000			86.24	3.15		0.19	1.06	1.48		1.24	6.64
230.000			86.02	3.18		0.17	1.06	1.48		1.26	6.83
220.000			85.83	3.21		0.14	1.07	1.48		1.28	7.00
210.000			85.65	3.25		0.10	1.08	1.48		1.30	7.15
200.000			85.48	3.29		0.06	1.08	1.48		1.32	7.29
190.000			85.33	3.34		0.02	1.09	1.48		1.34	7.40
186.060			85.28	3.36		0.00	1.09	1.48		1.35	7.44
180.000			85.20	3.36			1.09	1.48		1.36	7.51
170.000			85.09	3.35			1.09	1.48		1.38	7.60
160.000			84.99	3.35			1.09	1.48		1.41	7.69
150.000			84.90	3.34			1.09	1.48		1.44	7.75
140.000			84.82	3.33			1.09	1.48		1.47	7.81
Temp. (° C)	Liq.	Al_7Cr	Al	Al_6Mn	Al_3Fe	Alpha	Mg_2Si	E_AlCr-MgMn	Al_7Cu_2M	S_ Al_2CuMg	$MgZn_2$

Section 4A: 7020 and 7075 Experimental Chemistry and Microstructures

Table A4. Experimental Chemical analysis of 7020, and 7075 aerospace alloys, weight-%.

Alloy	Si	Fe	Cu	Mn	Mg	Cr	Zn	Ti	Zr	Imp.
7020-T651	0.10	0.26	0.16	0.25	1.24	0.17	4.47	0.03	0.13	0.78
7075-T7351	0.05	0.19	1.5	0.01	2.6	0.20	5.6	0.02	0.02	0.45
7075-T651	0.07	0.16	1.5	0.03	2.5	0.18	5.6	0.03	0.03	0.44

(see microstructures Figures A1-A3)

7020*; 7075†

* EN 10204/3.1 Inspection Certificate Technological Properties: (a) Aleris Al. Koblenz Gmbh 12-mm plate 01/29/2008, 25-mm plate 01/11/2007, and 50-mm plate 06/14/2007; and (b) Alcan Al. Valais (Sierre) 40-mm plate 01/09/2008.

† Chinella, J. F.; Jones, T. *Evaluation of Commercial Aluminum Alloys for Armor and Vehicle Upgrade*; ARL-TR-4596; U.S. Army Research Laboratory: Aberdeen Proving Ground, MD, September 2008.

Microstructures of 7020-T651, 7075-T651, and 7075-T7351 Aluminum Alloys: Ingot Cast, Rolled to Plate, Solution Treated, Quenched, and Artificial Age-Hardened

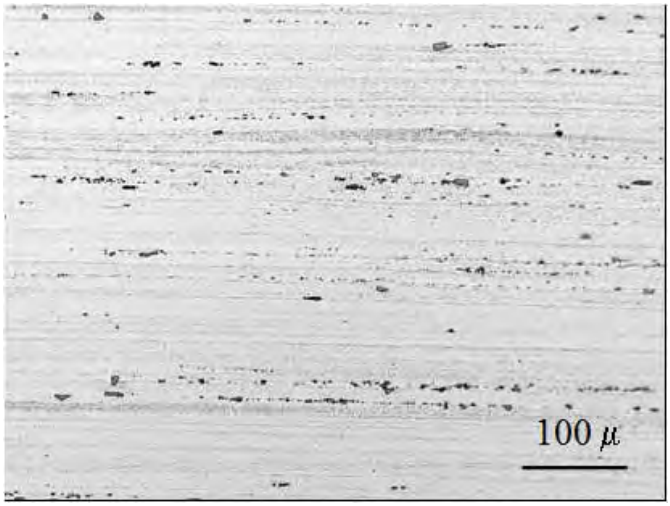

Figure A1. 7020-T651, 25 mm plate, longitudinal-transverse (L-T) plane.

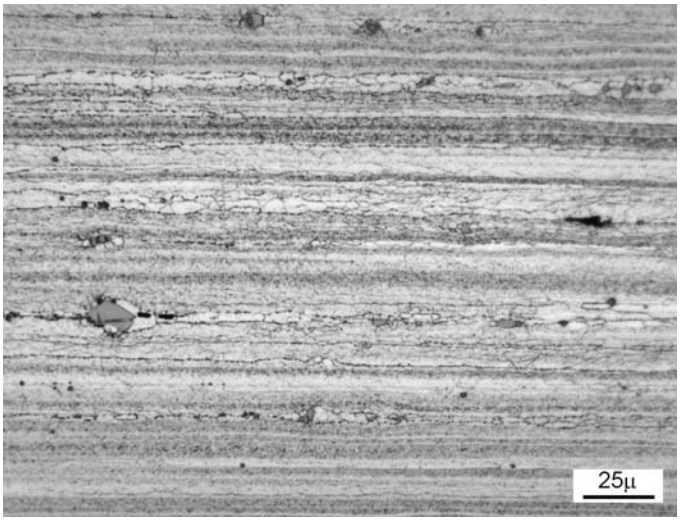

Figure A2. 7075-T651, 25 mm plate, L-T plane.

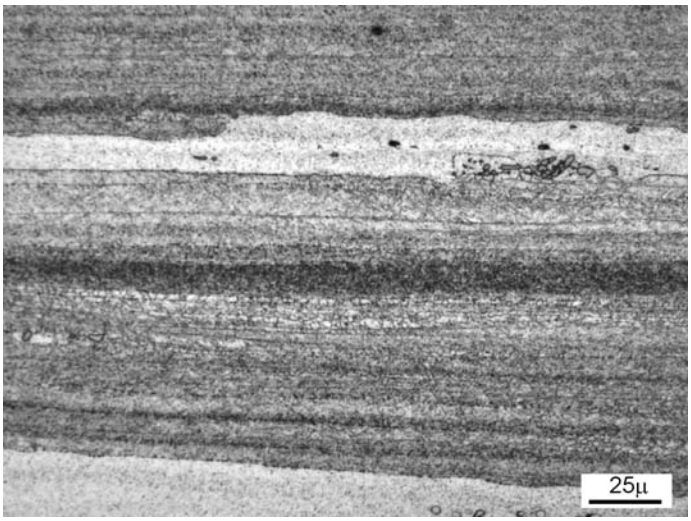

Figure A3. 7075-T7351, 25 mm plate, L-T plane.

NO. OF COPIES	ORGANIZATION
1 (PDF only)	DEFENSE TECHNICAL INFORMATION CTR DTIC OCA 8725 JOHN J KINGMAN RD STE 0944 FORT BELVOIR VA 22060-6218
1	DIRECTOR US ARMY RESEARCH LAB IMNE ALC HRR 2800 POWDER MILL RD ADELPHI MD 20783-1197
1	DIRECTOR US ARMY RESEARCH LAB RDRL CIO LL 2800 POWDER MILL RD ADELPHI MD 20783-1197
1	DIRECTOR US ARMY RESEARCH LAB RDRL CIO MT 2800 POWDER MILL RD ADELPHI MD 20783-1197
1	DIRECTOR US ARMY RESEARCH LAB RDRL D 2800 POWDER MILL RD ADELPHI MD 20783-1197

NO. OF COPIES ORGANIZATION

3 CDR US ARMY TACOM
AMSTA TR S
T FURMANIAK
L FRANKS
D TEMPLETON
MS 263
WARREN MI 48397-5000

1 CDR US ARMY TACOM
AMSTA TR R
D HANSEN
WARREN MI 48397-5000

1 PM HBCT
SFAE GCS HBCT S
J ROWE MS 506
6501 E 11 MILE RD
WARREN MI 48397-5000

2 US ARMY RSRCH DEV & ENGRG CTR
AMSRD NSC IPD B
P CUNNIFF
J WARD
KANSAS ST
NATICK MA 01760-5019

5 NATL GROUND INTLLGNC CTR
D EPPERLY
T SHAVER
T WATERBURY
W GSTATTENBAUER
D DOBROWLSKI
2055 BOULDERS RD
CHARLOTTESVILLE VA 22091-5391

2 PM MRAP
J PEREZ (JPO)
E BARSHAW
SFAE CSS MRE MS 298
6501 E 11 MILE RD
BLDG 229
WAREN MI 48397-5000

1 PM BFVS
ATTN SFAE GCSS W BV S
M KING
WARREN MI 48397-5000

1 SANDIA NATL LAB
D CRAWFORD MS 0836 9116
PO BOX 5800
ALBUQUERQUE NM 87185-0307

NO. OF COPIES ORGANIZATION

1 NVL SURFC WARFARE CTR
CARDEROCK DIV
R PETERSON
CODE 28
9500 MACARTHUR BLVD
WEST BETHESDA MD 20817-5700

2 LAWRENCE LIVERMORE NATL LAB
R LANDINGHAM L372
J REAUGH L282
PO BOX 808
LIVERMORE CA 94550

2 LOS ALAMOS NATL LAB
F ADDESSIO
M BURKETT
PO BOX 1663
LOS ALAMOS NM 87545

1 THE AIR FORCE RSRCH LAB
AFRL MLLMP
T TURNER
BLDG 655 RM 115
2230 TENTH ST
WRIGHT-PATTERSON AFB OH
45433-7817

1 AIR FORCE ARMAMENT LAB
AFATL DLJW
W COOK
EGLIN AFB FL 32542

4 UNIV OF TEXAS
INST FOR ADVNCD TECH
S BLESS
H FAIR
J HODGE
R SUBRAMANIAN
3925 W BRAKER LN
AUSTIN TX 78759-5316

1 UNIV OF DAYTON RSRCH INST
N BRAR KLA 14
300 COLLEGE PARK
DAYTON OH 45469-0182

2 SOUTHWEST RSRCH INST
C ANDERSON
J WALKER
6220 CULEBRA RD
SAN ANTONIO TX 78238

NO. OF COPIES	ORGANIZATION
3	US DEPT OF ENERGY NETL J HANSEN P TURNER P KING 1450 QUEEN AVE SW ALBANY OR 97321-2198
1	ALCAN ROLLED PRODUCTS J OFFER 39111 W SIX MILE RD STE 173 LIVONIA MI 48152
1	ALCOA DEFENSE R HEIPLE 100 TECHNICAL DR ALCOA CENTER PA 15069-0001
2	ALLVAC OREMET FACLTY J KOSIN B MAHONEY 530 34TH AVE SW PO BOX 460 ALBANY OR 97321
2	AM GENERAL S GRATE J RITTER 12200 HUBBARD RD PO BOX 3330 LIVONIA MI 48151-3330
1	ARMORWORKS W PERCIBALLI 305 N 54TH ST CHANDLER AZ 85226
2	ARCELOR MITTAL STEEL USA T DEAN J BABICH 139 MODENA RD PO BOX 3001 COATESVILLE PA 19320-0911
2	ATI ALLEGHENY LUDLUM R BAILEY G SWIATEK 500 GREEN ST WASHINGTON PA 15301
1	ATI DEFENSE A NICHOLS 500 GREEN ST WASHINGTON PA 15301
1	ATI DEFENSE L MARTIN 1600 OLD SALEM RD NE ALBANY OR 97321-0460
1	BROWN UNIV DIV OF ENGRG R CLIFTON PROVIDENCE RI 02912
3	BAE LAND COMBAT SYS B KARIYA M MIDDIONE D SCHADE 1205 COLEMAN AVE SANTA CLARA CA 95050
4	BAE SECURITY AND SURVIVABILITY M REYNOLDS M BOCZAK T RUSSELL M BERNING 9113 LE SAINT DR FAIRFIELD OH 45014
2	BAE ADVANCED CERAMICS R PALICKA G NELSON 991 PARK CTR DR VISTA CA 92083-7933
1	BAE SYSTEMS STEEL PRODUCTS J DORSCH 2101 W 10TH ST ANNISTON AL 36201
2	BAE LAND COMBAT SYS E BRADY R JENKINS 1100 BAIRS RD YORK PA 17405-1512
1	UNITED DEFNS LIMITED PARTNERS GROUND SYS DIV K STRITTMATTER PO BOX 15512 YORK PA 17405-1512

NO. OF COPIES ORGANIZATION

2 BAE SECURITY AND SURVIVABILITY
R MONKS
V KELSEY
7822 S 46TH ST
PHOENIX AZ 85044

1 CARPENTERSTEEL
P THOMPSON
PO BOX 14662
READING PA 19612-4662

2 CERADYNE INC
M KING
M NORMANDIA
3169 RED HILL AVE
COSTA MESA CA 92626

1 CLIFTON STEEL CO
J SOMOGYI
16500 ROCKSIDE RD
MAPLE HTS OH 44137

1 CONCURRENT TECHNOLOGIES
J PICKENS
100 CTC DR
JOHNSTOWN PA 15904-1935

1 CYPRESS INTRNTL
R ASOKLIS
47345 FEATHERED CT
SHELBY TOWNSHIP MI 48315

1 DAMILER TRUCKS NA LLC
R ENGEL
2477 DEERFIELD DR
FORT MILL SC 29715

1 INTERNATL RSRCH ASSN
D ORPHAL
4450 BLACK AVE
PLEASANTON CA 94566

1 IDEAL INNOVATIONS INC
R KOCHER
4601 N FAIRFAX ST
STE 1130
ARLINGTON VA 22203

1 KAIROS PARTNERS INC
D AKERS
PO BOX 3629
CHESTER VA 23831-3629

NO. OF COPIES ORGANIZATION

4 GDLS
W BURKE MZ436 21 24
G CAMPBELL MZ436 30 44
J ERIDON MZ436 21 24
W HERMAN MZ435 01 24
38500 MOUND RD
STERLING HTS MI 48310-3200

1 KAISER ALUMINUM
J SANDERSON
27422 PORTOLA PKWY
STE 350
FOOTHILL RANCH CA 92610-0892

1 MAGNESIUM ELEKTRON NA
R DELORME
1001 COLLEGE ST
PO BOX 258
MADISON IL 62060

1 FORCE PROTECTION INDUST INC
V JOYNT
9801 HWY 78
LADSON SC 29456

1 MISTRAL
E BANAI
7910 WOODMONT AVE
STE 820
BETHESDA MD 20814

1 EVRAZ OREGON STEEL
J ROSMUS
14400 N RIVERGATE BLVD
PORTLAND OR 97203

2 OSHKOSH DEFENSE
D PELCO
M IVEY
370 W WAUKAU
PO BOX 2566
OSHKOSH WI 54903-2566

1 FOSTER-MILLER
R SYKES
195 BEAR HILL RD
WALTHAM MA 02451

1 RMI TITANIUM CO
W PALLANTE
PO BOX 269
1000 WARREN AVE
NILES OH 44446

NO. OF COPIES ORGANIZATION

2 SOUTHWEST RSRCH INST
T HOLMQUIST
G JOHNSON
5353 WAYZATA BLVD STE 607
MINNEAPOLIS MN 55416

2 TENCATE ADVNCD COMPOSITES
D PUCKETT
E SIEFFERT
18410 BUTTERFIELD RD
MORGAN HILL CA 95037

2 TIMET
J FANNING
S FOX
PO BOX 2128
HENDERSON NV 89009

1 TIMET
M GUSTIN
224 VALLEY CREEK BLVD
EXTON PA 19341

2 UNIV OF CA SAN DIEGO
DEPT OF APPL MECH & ENGR
SVC RO11
S NEMAT NASSER
M MEYERS
LA JOLLA CA 92093-0411

1 US MILITARY ACADEMY
MATH SCI CTR EXCELLENCE
MADN MATH
THAYER HALL
WEST POINT NY 10996-1786

2 ALUMINUM CO OF AMERICA
ALCOA TECHNICAL CTR
DEV ENGRNG AND RSRCH
R RIOJA
C J WARREN
100 TECHNICAL DR
ALCOA CTR PA 15069-001

1 KAISER ALUMINUM
R D PARKINSON
STE 350
27422 PORTULA PKWY
FOOTHILL RANCH CA 92610-2831

NO. OF COPIES ORGANIZATION

1 CTC UNITED DEFNS
MGR MTRLS TECHLGY
J DORSCH
1205 COLEMAN AVE
SANTA CLARA CA 95050

1 MTRLS TECHNLGY
BAE SYSTEMS SANTA CLARA
T J DORSCHE
1205 COLEMAN AVE
SANTA CLARA CA 95050

1 THERMO CALC SOFTWARE
P MASON
4160 WASHINGTON RD
STE 230
MCMURRY PA 15317

1 ALCAN ROLLED PRODUCTS
S MOSSER
CENTURY RD PO BOX 68
RAVENSWOOD WV 26164-0068

ABERDEEN PROVING GROUND

1 DIR USAMSAA
AMSRD AMS D
BLDG 392
APG MD 21005

1 CDR USATEC
STEAC LI LV
E SANDERSON
BLDG 400
APG MD 21005

1 US ARMY EVAL CTR
TEAE SVB
M SIMON
4120 SUSQUEHANNA AVE
APG MD 21005-3013

71 DIR USARL
RDRL ROE M
S MATHAUDHU
RDRL SL
R COATES
RDRL SLB
BOWEN
RDRL WM
J MCCAULEY

NO. OF COPIES ORGANIZATION

RDRL WML B
J NEWILL
RDRL WML H
T FARRAND
L MAGNESS
D SCHEFFLER
S SCHRAML
R SUMMERS
RDRL WMM
J BEATTY
R DOWDING
RDRL WMM A
J SANDS
RDRL WMM B
B CHEESEMAN
G GAZONAS
RDRL WMM D
R CARTER
E CHIN
K CHO
W ROY
R SQUILLACIOTI
S WALSH
RDRL WMM E
J LASALVIA
P PATEL
RDRL WMM F
J CHINELLA
L KECSKES
J MONTGOMERY
D SNOHA
RDRL WMP
S SCHOENFELD
RDRL WMP A
C HUMMER
B RINGERS
RDRL WMP B
S BILYK
D CASEM
J CLAYTON
D DANDEKAR
M GREENFIELD
C HOPPEL
Y HUANG
B LEAVY
M RAFTENBERG
M SCHEIDLER
T WEERASOORIYA
RDRL WMP C
T BJERKE
S SEGLETES
W WALTERS

NO. OF COPIES ORGANIZATION

RDRL WMP D
A BARD
R DONEY
M DUFFY
T HAVEL
V HERNANDEZ
S HUG
M KEELE
D KLEPONIS
H MEYER
J RUNYEON
B SCOTT
K STOFFEL
RDRL WMP E
P BARTKOWSKI
S BARTUS
M BURKINS
D GALLARDY
W GOOCH
D HACKBARTH
E HORWATH
T JONES
C KRAUTHAUSER
B LOVE
M LOVE
D SHOWALTER
RDRL WMP F
N GNIAZDOWSKI
R GUPTA
RDRL WMP G
R BANTON

NO. OF COPIES ORGANIZATION

1 ALCOA EUROPE
G BEVAN
PO BOX 383
KITTS GREEN RD KITTS GREEN
BIRMINGHAM B33 9QR
UNITED KINGDOM

1 ALCOA EUROPE
A ARMIGLIATO
ALCOA TRASFROMAZIONI
VIA DELL'ELETTRONICA 31
30030 FUSINA (VENEZIA)
ITALY

3 ARCELOR MITTAL
INDUSTEEL CREUSOT
E DERASSAT
S CORRE
D HERITIER
56 RUE CLEMENCEAU
BP 19
71201 LE CREUSOT CEDEX
FRANCE

2 ARMOR AUSTRALIA
A FAIRBAIRN
H OLDFIELD
2/461 THE BOULEVARDE
KIRRAWEE NSW 2232
AUSTRALIA

3 BAE SYSTEMS HÄGGLUNDS AB
T GUSTAFSSON
L PETTERSSON
A BERGKVIST
SE-891 82 ÖRNSKÖLDSVIK
SWEDEN

2 DSTO
WEAPONS SYSTEMS DIV
N BURMAN
J ANDERSON
PO BOX 1500
EDINBURGH SA 5111
AUSTRALIA

2 DEFENSE RESEARCH AGENCY
B JAMES
B SHRUBSALL
PORTON DOWN
SALISBURY WTTTS SP04 OJQ
UNITED KINGDOM

NO. OF COPIES ORGANIZATION

1 DEFENCE RESEARCH AND
DEVELOPMENT-VALCARTIER
R DELAGRAVE
2459 PIE XI NORTH
VAL-BELAIR QC G3J 1X5
CANADA

1 DEUTSCH FRANZOSISCHES
FORSCHUNGSINSTITUT ST LOUIS
CEDEX 5 RUE DU
GENERAL CASSAGNOU
F 68301 SAINT LOUIS
FRANCE

3 FRANHOFER INSTITUT FUR
KURZZEITDYNAMIK
ERNST MACH INSTITUT
E STRASSBURGER
K THOMA
M WICKERT
ECKERSTRASSE 4
D 79 104 FREIBURG
GERMANY

2 GD LAND SYSTEMS CANADA
P GALLAGHER
K BENARD
PO BOX 7003
LONDON ONTARIO N5Y 6L8
CANADA

1 INDUSTRIE BITOSSI
R ROVAI
VAI PIETRAMARINA 53
I-50053 SOVIGLIANA-VINCI
ITALY

1 INGENIEURBURO DEISENROTH
F DEISENROTH
AUF DE HARDT 33 35
D 5204 LOHMAR 1
GERMANY

3 INST FOR PROBLEMS IN MATLS SCI
B GALANOV
V KARTUZOV
Y MILMAN
3 KRHYZHANOVSKY STR
252142 KIEV 142
UKRAINE

NO. OF COPIES ORGANIZATION

2 NORDMETALL GBR
L MEYERS
S ABDEL-MALEK
EIBENBERG
EINSIEDLER STGR 18H
D 09235 BURKHARDSDORF
GERMANY

1 NATL DEFENCE HDQRTRS
PMO LAV A HODAK
OTTOWA ONTARIO KIA OK2
CANADA

1 RAFAEL
D YAZIV
PO BOX 2250
HAIFA 31021
ISRAEL

1 ROYAL NETHERLANDS ARMY
JHOENEVELD
V D BURCHLAAN 31
PO BOX 90822
2509 LS THE HAGUE
NETHERLANDS

1 RIMAT
M RAVID
8B SIMTAT HAYEREK
HOD HASHARON 45264
ISRAEL

2 RUKKI
V-M MANNER
J ASUNMAA
RAUTARUUKINTIE 155
PO BOX 93
FI 92101 FAAHE
FINLAND

2 DEFENCE MATERIEL ADMIN
WEAPONS DIRECTORATE
A BERG
R LINSTRÖM
S 11588 STOCKHOLM
SWEDEN

1 SECRAB
B JANZON
PO BOX 97
SE-147 22 TUMBA
SWEDEN

NO. OF COPIES ORGANIZATION

1 SSAB OXELÖSUND AB
ARMOR PLATE MANAGER
SE-613 80 OXELÖSUND
SWEDEN

4 SWEDISH FOI
P LUNDBERG
J OTTOSSON
E LIDEN
L WESTERLING
SE-147 25 TUMBA
SWEDEN

2 TNO DEFENCE SECURITY & SAFETY
A DIEDEREN
F T M VAN WEGEN
LANGE KLEIWEG 137
PO BOX 45
2280 AA RIJSWIJK
THE NETHERLANDS

1 TDW EADS
M HELD
PO BOX 1340
SCHROBENHAUSEN D 86523
GERMANY

1 SURREY TECHNLGY CENTRE
J PHILLIPPE SCHILLÉ
40 OCCAM RD
GUILFORD GU2 7YG
UNITED KINGDOM